PHYSICAL REVIEW E **92**, 032104 (2015)

Dispersion of overdamped diffusing particles in channel flows coupled to transverse acoustophoretic potentials: Transport regimes and scaling anomalies

Massimiliano Giona[1,*] and Fabio Garofalo[2,†]
[1]*Dipartimento di Ingegneria Chimica, Materiali, Ambiente, La Sapienza Università di Roma, Via Eudossiana 18, 00184 Roma, Italy*
[2]*Department of Biomedical Engineering, Lund University, Ole Römers Väg 3, 22363 Lund, Sweden*

(Received 15 July 2015; published 4 September 2015)

We address the dispersion properties of overdamped Brownian particles migrating in a two-dimensional acoustophoretic microchannel, where a pressure-driven axial Stokes flow coexists with a transverse acoustophoretic potential. Depending on the number and symmetries of the stable nodal points of the acoustophoretic force with respect to the axial velocity profile, different convection-enhanced dispersion regimes can be observed. Among these regimes, an anomalous scaling, for which the axial dispersion increases exponentially with the particle Peclét number, is observed whenever two or more stable acoustophoretic nodes are associated with different axial velocities. A theoretical explanation of this regime is derived, based on exact moment homogenization. Attention is also focused on transient dispersion, which can exhibit superballistic behavior $\langle (x-\langle x\rangle)^2\rangle \sim t^3$, x being the axial coordinate.

DOI: 10.1103/PhysRevE.92.032104 PACS number(s): 05.40.−a, 47.61.−k, 05.60.−k

I. INTRODUCTION

The interplay between stochastic Brownian fluctuations and deterministic fields plays a central role in modern physics with implications ranging from field theory [1] to soft matter and polymer physics [2], encompassing cosmological and astrophysical models [3] as well as atom physics [4]. The role of noise is central in determining macroscopic emergent features in the collective behavior of particle ensembles, as regards both the average transport properties and the dispersion behavior around the average motion. The availability of theoretical models that can predict transport regimes according to the structure of the deterministic drive and the nature and intensity of fluctuations can greatly facilitate the optimized design of a number of micro- and nanofluidic devices, such as micromixers, cell and DNA sorting devices, and active microsensors [5].

A primary distinction between classes of problems can be drawn depending on the nature of the deterministic drive that causes the average motion of the particle ensemble. If the drive stems from a vector potential, then the effective particle velocity expressing the average particle motion is also solenoidal. This is the case, for instance, of overdamped diffusing particles (tracers) subjected solely to Stokesian drag in an incompressible flow. In this case, the time-asymptotic average velocity of the particle ensemble equals the spatial average of the flow velocity, and interesting effects are only associated to deviations about the average motion. In the case where transport occurs in a bounded impermeable domain these deviations are responsible for convection-enhanced or chaos-enhanced mixing regimes, which arise from the cooperative interaction between deterministic and stochastic motion and that are quantitatively defined by the spectral structure of the advection-diffusion operator [6]. Besides, this synergetic interaction shows its effect even in unbounded domains where large-scale dispersion of particle ensembles is typically enhanced over the bare particle diffusivity. Classical examples are Taylor-Aris axial dispersion in laminar flows through straight channels [7] and the peculiar behavior of the effective dispersion tensor associated with passive tracers transported in two-dimensional spatially periodic incompressible flows, where different dispersion regimes can be predicted depending on the rotation number of the mean sweep flow [8,9].

On the other hand, if the particle velocity stems from a scalar potential (i.e., it is irrotational), then long-time averages of particle velocity and spatial averages of the deterministic drive need not coincide, and several interesting and peculiar phenomena have been observed for both stationary and time-periodic potentials, such as stochastic resonance [10], noise rectification in time-periodic landscapes (Brownian motors) [11], and giant diffusion (in tilted potentials) [12], especially in the presence of disorder [13].

With an eye to the Hodge-Helmholtz decomposition of vector fields $\mathbf{v}(\mathbf{x})$ into a solenoidal $\mathbf{v}_{\rm sol}(\mathbf{x})$, and irrotational $\mathbf{v}_{\rm irr}(\mathbf{x})$ component [14],

$$\mathbf{v}(\mathbf{x}) = \mathbf{v}_{\rm sol}(\mathbf{x}) + \mathbf{v}_{\rm irr}(\mathbf{x}) \tag{1}$$

$$\nabla \cdot \mathbf{v}_{\rm sol} = 0\,, \quad \mathbf{v}_{\rm sol} = \nabla \times \mathbf{A}\,, \qquad \nabla \times \mathbf{v}_{\rm irr} = 0\,, \quad \mathbf{v}_{\rm irr} = \nabla \phi\,,$$

most of the literature on Brownian dynamics, particle dispersion, and/or mixing has been focused either on purely solenoidal or purely irrotational (potential) flows. There are only few exceptions to this tendency, such as the recent work by Cerbelli [15] reporting the logarithmic scaling of the dispersion coefficient as a function of the Peclét number for Brownian particles moving in a critical array of cylindrical obstacles under the action of a constant force (which can be viewed both as solenoidal as well as irrotational) and the investigation of dispersion in the same setting for various (noncritical) geometries by Ghosh *et al.* [16].

The present work analyzes the dispersion properties for the overdamped motion of particles in a parallel channel flow where a transverse potential is superimposed to the Stokesian (incompressible) axial velocity profile. Beyond the theoretical interest in dispersion theory, this model describes the (ideal) dynamics of micro- and nanoparticle motion

---

[*] Corresponding author: massimiliano.giona@uniroma1.it

[†] fabio.garofalo@bme.lth.se

in acoustophoretic microflow devices, where the transverse potential accounts for the action of the acoustophoretic force acting on particles, which is gaining more and more interest as a method for an effective control and separation of particles [17–19]. The practical feasibility of this depends on the structural properties of the particles, which, in biological suspensions, are related to the biophysical properties of the cells. In this context, one of the most promising applications is the splitting of a continuous stream of cells into healthy and neoplastic subpopulations based upon the different compressibility that the cancerous cells possess compared to the healthy ones [20].

The interaction among axial flow, acoustophoretic force, and thermal fluctuations determines three emerging phenomena, namely (i) the relaxation of particle number density towards the stationary (Frobenius) distribution in the transverse direction to the flow, (ii) the asymptotic (long-term or large-distance) axial dispersion, and (iii) the anomalous intermediate (transient) effects in the particle mean-square displacement as a function of time. These three phenomena are next thoroughly addressed both analytically and numerically. Exact moment homogenization, namely the application of the macrotransport theory developed by Brenner and coworkers [21–23] to this class of channel flows, is used to derive the asymptotic (long-term or large-distance) dispersion properties.

We show that in the long-term or large-distance limit, axial dispersion displays three different regimes, depending on the spatial structure of the acoustophoretic force (essentially, on the number of its stable nodal points), and on the value of the axial velocity at these nodes. An interesting regime, which, to the best of our knowledge, has never been observed before, occurs when the acoustophoretic potential displays two or more stable nodes at which the axial flow profile attains different velocity values. In this case, an exponential dependence of the axial dispersion coefficient on the particle Peclét number can be observed and predicted.

Of theoretical and practical interest is also the transient axial dispersive behavior. We show that an anomalous, superballistic regime (i.e., the mean-squared displacement grows as the third power of time) can be observed for certain particle distributions entering the inlet cross section of the device.

The article is organized as follows. Section II describes succinctly the modeling of acoustophoretic channel microdevices and derives the system of Langevin and Fokker-Planck equations describing Brownian particle motion within the overdamped approximation. Section III addresses homogenization via moment analysis for this class of channel flows and derives a bound for the asymptotic axial dispersion coefficient. Section IV analyzes particle distribution in the transverse direction, whose dynamics is decoupled from axial motion, and discusses the related physical properties (i.e., the behavior of the effective axial velocity). Section V develops the asymptotic analysis of axial dispersion regimes supporting the theoretical predictions (derived from moment analysis developed in Sec. IV) with Langevin simulations. A detailed analysis of the equation for the steady field controlling dispersion properties (cfr. the b field) is developed, providing a fully analytic and simple interpretation of the phenomenological dispersion properties observed. Section VI addresses transient dispersion effects and provides a simple interpretation of the super-ballistic phenomena occurring for particular classes of the acoustophoretic potential and for some inlet conditions.

II. PHYSICAL MOTIVATION: ACOUSTOPHORETIC FLOW DEVICES

Free-flow acoustophoretic microdevices have been recently proposed and investigated for particle manipulation and separation in steady channel flows, exploiting particle interaction with a pressure wave transverse to the flow. These devices have been shown to provide an accurate control over particle trajectories while being easy to produce and inducing relatively low stresses on suspended particles and cells [24] when compared to other techniques.

The flow-particle interaction, which allows manipulation and separation, derives from the acoustophoretic force acting on particles, which depends on fluid and particle properties, such as viscosity, compressibility, and density [25–29]. The transition between inviscid and viscous behavior for particle motion driven by an acoustophoretic force, is accounted for by the *acoustic boundary layer thickness* $\delta = \sqrt{\frac{2\eta_l}{\rho_l \omega}}$, where η_l is the viscosity of the liquid ($\eta_{\text{water}} \simeq 10^{-3}$ Pa s), ρ_l the liquid density ($\rho_{\text{water}} = 10^3$ kg m^{-3}), and ω the angular frequency of the acoustic wave, $\omega = 2\pi f$. For instance, for an ultrasonic acoustic wave propagating in water at room temperature, the acoustic boundary layer thickness attains a value order of microns. This implies that the action of ultrasonic waves on particles of radius larger than $3 \div 5$ μm can be described by means of the inviscid theory. This is the case of cells, whose diameter falls in the range $a_{\text{cell}} = 1 \div 10$ μm with exceptional cases around 100 μm. Conversely, for nanoparticles, i.e., $a_{\text{nano}} = 1 \div 100$ nm, the evaluation of the momentum transfer between the fluid surrounding the particle and the particle must explicitly take into account dissipation effects due to viscosity in the wave propagation. Furthermore, viscous dissipation has been proved responsible for the generation of recirculating cross-sectional vortices in three-dimensional models [30].

A dimensionless parameter accounting for the effect of the viscosity is the dimensionless boundary layer thickness $\tilde{\delta} = \delta/a$, which attains the values $\tilde{\delta}_{\text{cell}} = 10^{-3} \div 10^{-1}$ and $\tilde{\delta}_{\text{nano}} = 1 \div 10^2$ for micrometer and nanometer sized particles, respectively. When the dimensionless acoustic boundary layer thickness results $\tilde{\delta} \ll 1$, inviscid theory can be applied.

The acoustic radiation force also depends upon the ratio $\tilde{\kappa}$ of the compressibility of the fluid κ_f to that of the particles κ_p, where κ is give by $\kappa = -V^{-1}(\partial_p V)_T$. For instance, the compressibility of water is $\kappa_{\text{water}} \simeq 450$ TPa^{-1}, while that of cells is in general slightly less so $\tilde{\kappa}_{\text{cell}} \lesssim 1$. Different kinds of micro-sized particles can be processed in acoustophoretic devices depending on the purpose. For example, polystyrene beads, which are used to indirectly measure the viscosity of the liquid within which they migrate, are characterized by $\kappa_{\text{ps}} \simeq$ 150 TPa^{-1}. For particles possessing sizes between nanometers and micrometers, Brownian fluctuations should also be taken into account. Effective particle diffusivity can be estimated via the Stokes-Einstein equation $D = \frac{k_B T}{6\pi \eta_l a}$, where T is the temperature. At room temperature, the effective diffusivity of the cells is order of $D_{\text{cell}} \simeq 10^{-13} \div 10^{-14}$ m^2 s^{-1}, while for $a = a_{\text{nano}}$ the effective diffusivity results $D_{\text{nano}} \simeq 10^{-10} \div 10^{-12}$ m^2 s^{-1}.

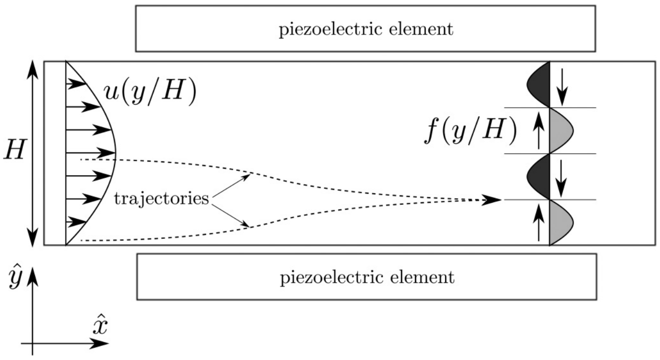

FIG. 1. Schematic picture of a free-flow acoustophoretic device.

A. Particle motion in an acoustophoretic channel

This section reviews briefly the equations governing particle transport in a free-flow acoustophoretic channel. A two-dimensional model is assumed, see Fig. 1.

The description of the acoustophoretic force is based upon the knowledge of the *acoustophoretic contrast factor* that, as developed in Ref. [29], is given by:

$$\Phi(\tilde{\kappa},\tilde{\rho},\tilde{\delta}) = \tfrac{1}{3} f_1(\tilde{\kappa}) + \tfrac{1}{2}\mathrm{Re}[f_2(\tilde{\rho},\tilde{\delta})]. \tag{2}$$

The quantity $f_1(\tilde{\kappa}) = 1 - \tilde{\kappa}$ is the *monopole scattering coefficient*, while

$$f_2(\tilde{\rho},\tilde{\delta}) = \frac{2[1-\gamma(\tilde{\delta})](\tilde{\rho}-1)}{2\tilde{\rho}+1-3\gamma(\tilde{\delta})} \tag{3}$$

is the *dipole scattering coefficient*, where $\gamma(\tilde{\delta}) = -\frac{3}{2}[1 + i(1+\tilde{\delta})]\tilde{\delta}$. For a stationary plane wave orthogonal to the channel axis, the acoustophoretic force $f(y/H)$ can be expressed as [29]:

$$f(y/H) = \frac{(2\pi)^2 \Phi a^3 E_a k}{H} \sin\left(\frac{2\pi k y}{H}\right), \tag{4}$$

where H is the channel width, k the number of half-wavelengths [note that the pressure wave results $p \sim \cos(k\pi y/H)$], and $E_a \sim 10^1 \div 10^3 \mathrm{J\,m^{-3}}$ is the acoustic energy.

Consider a two-dimensional channel with a transverse characteristic size H, and indefinitely extended in the axial direction, see Fig. 1, in which the fluid moves with an axial velocity $u(y/H)$ and a pressure wave generates the transverse acoustophoretic force $f(y/H)$. For a Poiseuille flow $u(y/H) = V\,6\,[(y/H) - (y/H)^2]$, where V is the mean axial velocity.

Considering the Stokes drag acting of the particles in a viscous fluid, the stochastic dynamics governing particle motion is described by the system of stochastic (Langevin) differential equations:

$$m_p d\dot{x} = -6\pi\eta a[\dot{x} - V\,u(y/H)]\,dt + \alpha_T\,dw_x(t), \tag{5a}$$

$$m_p d\dot{y} = -6\pi\eta a\dot{y}\,dt + \frac{(2\pi)^2\Phi a^3 E_a k}{H}\sin\left(\frac{2\pi k y}{H}\right)dt + \alpha_T\,dw_y(t), \tag{5b}$$

where $\dot{x} = dx/dt$, $\dot{y} = dy/dt$, α_T is the intensity of thermal fluctuations, and $w_x(t)$ and $w_y(t)$ are two independent Wiener processes. Considering spherical particles, i.e., $m_p = \frac{4}{3}\pi a^3 \rho_p$, and making spatial coordinates and time dimensionless via the rescaling $x/H \to x$, $y/H \to y$, $tV/H \to t$, the system (5) can be recast the form:

$$\mu d\dot{x} = -[\dot{x} - u(y)]\,dt + \sqrt{2\varepsilon}dw_x(t), \tag{6a}$$

$$\mu d\dot{y} = [-\dot{y} + \nu\sin(2\pi k y)]\,dt + \sqrt{2\varepsilon}dw_y(t), \tag{6b}$$

where $\mu = \frac{2\rho_p a^2 V}{9\eta_f H}$ is the dimensionless mass of the particles, $\nu = \frac{(2\pi a)^2 \Phi E_a l}{6\pi\eta_f H V}$ the dimensionless acoustophoretic force intensity, and $\varepsilon = D/VH = 1/\mathrm{Pe}$ the reciprocal of the Peclét number Pe, related to α_T by the equation $\sqrt{2\varepsilon} = \sqrt{H/V}\alpha_T/6\pi\eta_f a H$. Henceforth, x, y, and t are dimensionless variables.

For physically admissible values of H and V used in microfluidic applications, the dimensionless mass of the particle is order of $\mu = 10^{-7} \div 10^{-1}$ for neutrally buoyant particles in water and $a = 10^{-9} \div 10^{-6}$ m. Therefore, it is reasonable to neglect the inertia in almost all of the cases and assume overdamped conditions, namely $\mu \simeq 0$. Correspondingly, the system (6) becomes:

$$dx(t) = u(y)\,dt + \sqrt{2\,\varepsilon}\,dw_x(t), \tag{7a}$$

$$dy(t) = \nu\sin(2\pi k y)\,dt + \sqrt{2\,\varepsilon}\,dw_y(t). \tag{7b}$$

The intensity of the dimensionless acoustophoretic force for cell-like particles is in the range $\nu = 10^{-2} \div 10^0$. For nanoparticles the estimate is slightly more difficult, mainly because the values of the parameters above introduced are subjected to significant variations, depending on the particle properties and the wave frequency. However, a reasonable estimate based upon the particle radius (observe that $\nu \sim a^2$) provides a value of ν that is of order $\nu \sim 10^{-6} \div 10^{-4}$. Finally, physically admissible value of the particle Peclét number ranges in the interval $\mathrm{Pe} = 10^2 \div 10^8$.

The dimensionless forward Fokker-Planck equation associated with the evolution of the particle density $p(x,y,t)$ reads as:

$$\partial_t p + u(y)\,\partial_x p + \nu\,\partial_y[\sin(2\pi k y)\,p] = \varepsilon\left(\partial_x^2 p + \partial_y^2 p\right). \tag{8}$$

Particle density is obviously normalized probabilistically, i.e., $\int_{-\infty}^{\infty} dx \int_0^1 p(x,y,t)\,dy = 1$. Equation (8) is equipped with regularity conditions for $|x| \to \infty$, meaning that $p(x,y,t)$ decays for $|x| \to \infty$ faster than any power of x, and with homogeneous Neumann boundary conditions at the solid walls of the channel (impermeable walls for particle transport), i.e.,

$$\partial_y p(x,y,t)|_{y=0,1} = 0. \tag{9}$$

III. CHANNEL-FLOW DISPERSION IN A TRANSVERSE POTENTIAL

Moment analysis of transport equations provides a simple and effective way to estimate effective transport parameter in dispersion problems in unbounded domains, alternative to multiple-scale expansion methods. Originally, this approach has been proposed by Aris [7] for incompressible channel-flow dispersion (the Taylor-Aris dispersion problem) and subsequently elaborated on further for a wealth of different transport problems by Brenner and coworkers [21,22]. These authors refer to it as the *macrotransport paradigm* for problems possessing local and global scale variables.

This section succinctly addresses the application of this approach to the compressible channel-flow problem associated with the Fokker-Planck equation (8), for which the local variable is simply the transverse coordinate y and the large-scale variable is the axial coordinate x.

In the long-term or large-distance limit, the marginal probability density function $p_x(x,t) = \int_0^1 p(x,y,t)\,dy$, averaged with respect to the cross-sectional coordinate y, satisfies an effective advection-diffusion equation with constant coefficients (see Ref. [31] for a rigorous mathematical setting of the convergence),

$$\partial_t p_x(x,t) = -V_e\,\partial_x p_x(x,t) + \varepsilon_e\,\partial_x^2 p_x(x,t), \tag{10}$$

where V_e is the effective axial velocity and ε_e is the reciprocal of the dispersion Peclét number

$$\varepsilon_e = \frac{D_e}{VH}, \tag{11}$$

D_e being the effective axial dispersion coefficient.

In order to obtain the expressions for V_e and ε_e, the hierarchy of local moments $\{p^{(n)}(y,t)\}_{n=0}^{\infty}$ associated with Eq. (8) can be introduced,

$$p^{(n)}(y,t) = \int_{-\infty}^{\infty} x^n\, p(x,y,t)\,dx, \quad n = 0,1,\ldots, \tag{12}$$

starting from which the hierarchy of global moments $\{m^{(n)}(t)\}_{n=0}^{\infty}$ is simply defined as the integral of the local moments over the channel cross section:

$$m^{(n)}(t) = \int_0^1 p^{(n)}(y,t)\,dy, \quad n = 0,1,\ldots. \tag{13}$$

Since $m^{(0)}(t) = 1$, by probability conservation and normalization, the time derivatives of the first- and second-order moments provide two simple estimators for V_e and ε_e, respectively. This is due to the fact that in the long-time or large-distance limit, it follows straightforwardly from Eq. (10) that:

$$\frac{dm^{(1)}(t)}{dt} = V_e, \tag{14}$$

$$\frac{dm^{(2)}(t)}{dt} = 2V_e\,m^{(1)}(t) + 2\varepsilon_e. \tag{15}$$

That said, the balance equations for the local moments can be obtained multiplying both sides of Eq. (8) by x^n and integrating over the axial variable:

$$\begin{aligned}\partial_t p^{(n)}(y,t) = {}& n\,u(y)\,p^{(n-1)}(y,t) + \mathcal{L}_y[p^{(n)}(y,t)]\\ &+ \varepsilon\,n(n-1)\,p^{(n-2)}(y,t),\end{aligned} \tag{16}$$

$n = 0,1,\ldots,$ where $\mathcal{L}_y$ is the transverse advection-diffusion operator,

$$\mathcal{L}_y[p^{(n)}(y,t)] = -\nu\,\partial_y[\sin(2\pi k y)\,p^{(n)}(y,t)] + \varepsilon\,\partial_y^2 p^{(n)}(y,t). \tag{17}$$

Equation (16), and, consequently, the transverse operator $\mathcal{L}_y$, are equipped with homogeneous Neumann conditions inherited from Eq. (9),

$$\partial_y p^{(n)}(y,t)|_{y=0,1} = 0, \tag{18}$$

for all $t > 0$, and $n = 0,1,\ldots$. Integrating Eq. (16) over the transverse section and observing that $\int_0^1 \mathcal{L}_y[p^{(n)}(y,t)]\,dy = 0$, the following expression for the time evolution of the global moments can be derived:

$$\frac{dm^{(n)}(t)}{dt} = n\int_0^1 u(y)\,p^{(n-1)}(y,t)\,dy + \varepsilon\,n(n-1)\,m^{(n-2)}(t). \tag{19}$$

So far, the analysis is exact. Let us now consider the long-time or large distance approximation for the estimate of the effective transport parameters. For $n = 0$, $p^{(0)}(y,t)$ satisfies the pure advection-diffusion equation

$$\partial_y p^{(0)}(y,t) = \mathcal{L}_y[p^{(0)}(y,t)], \tag{20}$$

equipped with the Neumann boundary conditions (18) at the channel walls. The spectral structure of $\mathcal{L}_y$ is fairly simple: (i) it admits a countable system of eigenvalues $\mathcal{L}_y[\psi_s(y)] = -\lambda_s\,\psi_s(y)$, $s = 0,1,\ldots$; (ii) all the eigenvalues are real, as $\mathcal{L}_y$ can be mapped into an Hermitian operator, by transforming $\mathcal{L}_y$ into an one dimensional Schrödinger operator; (iii) ordering the eigenvalues so $\lambda_0 < \lambda_1 \leqslant \lambda_2 \leqslant \cdots$, the first eigenvalue $\lambda_0 = 0$ is not degenerate and corresponds to probability conservation, while all the other eigenvalues $-\lambda_s$, $s = 1,2,\ldots$ are negative; and (iv) since $e^{\mathcal{L}_y}$ is a positive operator, the first eigenfunction $\psi_0(y)$ associated with the conservation eigenvalue $\lambda_0 = 0$ of $\mathcal{L}_y$ can be always chosen so $\psi_0(y) \geqslant 0$ (Frobenius theorem).

Therefore, the solution of Eq. (20) can be expressed as:

$$p^{(0)}(y,t) = \psi_0(y) + \mathcal{O}(e^{-\lambda_1 t}), \tag{21}$$

i.e., it asymptotically converges towards the conservation eigenfunction $\psi_0(y)$, $\mathcal{L}_y[\psi_0(y)] = 0$, that corresponds to the equilibrium transverse particle distribution. $\psi_0(y)$ by normalization is such that $\int_0^1 \psi_0(y)\,dy = 1$ and is referred to as the *Frobenius distribution* (or eigenfunction) of the transverse advection-diffusion operator. From Eq. (19) for $n = 1$ it follows:

$$\frac{dm^{(1)}(t)}{dt} = \int_0^1 u(y)\,p^{(0)}(y,t)\,dy. \tag{22}$$

The substitution of the asymptotic expression (21) into Eq. (22) provides the estimate for the effective axial velocity, namely

$$V_e = \int_0^1 u(y)\,\psi_0(y)\,dy, \tag{23}$$

that corresponds to the average of the axial velocity profile with respect to the Frobenius distribution $\psi_0(y)$.

Next consider the first-order local moment $p^{(1)}(y,t)$ that satisfies Eq. (16) for $n = 1$, i.e.,

$$\partial_t p^{(1)}(y,t) = \mathcal{L}_y[p^{(1)}(y,t)] + u(y)\,p^{(0)}(y,t). \tag{24}$$

Since $V_e \neq 0$, it is expected from Eq. (22) that $p^{(1)}(y,t)$ grows asymptotically as the first power of t. Therefore, the solution of Eq. (24) can be expressed as:

$$p^{(1)}(y,t) = \psi_0(y)[V_e t + b(y)] + \mathcal{O}(e^{-\lambda_1 t}), \tag{25}$$

where the steady field $b(y)$ can be determined by enforcing that Eq. (25) is a solution of Eq. (24). This provides the following balance equation for $b(y)$:

$$\mathcal{L}_y[\psi_0(y)\,b(y)] = \psi_0(y)[V_e - u(y)]. \tag{26}$$

Equation (26) is equipped with homogeneous Neumann boundary conditions

$$\partial_y(\psi_0(y)\,b(y))|_{y=0,1} = 0, \tag{27}$$

deriving from Eq. (18), which can be rewritten as $\partial_y b(y)|_{y=0,1} = 0$. Since the forcing term at the right-hand side of Eq. (26) possesses zero mean, Eq. (26) admits a solution. Indeed, if $\overline{b}(y)$ is a particular solution of Eq. (26) and C is a constant, then $b(y) = \overline{b}(y) + C$ is also a solution of Eq. (26), i.e., there are infinitely many solutions of Eq. (26) equipped with impermeable Neumann conditions differing from each other by an additive constant. This multiplicity of solutions is completely immaterial in the asymptotic estimate of the dispersion coefficient (as discussed below).

The long-time or large-distance expression for $m^{(2)}(t)$ follows by substituting the asymptotic expression (25) for $p^{(1)}(y,t)$ into Eq. (19) for $n = 2$, neglecting the exponentially vanishing contributions and using the identity $m^{(0)}(t) = 1$:

$$\frac{dm^{(2)}(t)}{dt} = 2\,V_e^2\,t + 2\int_0^1 u(y)\,\psi_0(y)\,b(y)\,dy + 2\,\varepsilon. \tag{28}$$

Since $m^{(1)}(t) = V_e t + \int_0^1 \psi_0(y)\,b(y)\,dy$, the latter expression can be rewritten as:

$$\frac{dm^{(2)}(t)}{dt} = 2V_e\,m^{(1)}(t) + 2\int_0^1 \psi_0(y)\,[u(y) - V_e]\,b(y)\,dy + 2\,\varepsilon, \tag{29}$$

where $b(y)$ is any solution of Eq. (26) satisfying the homogeneous Neumann boundary conditions. The comparison of Eq. (29) with Eq. (15) provides the expression for ε_e, namely:

$$\varepsilon_e = \varepsilon + \int_0^1 \psi_0(y)[u(y) - V_e]\,b(y)dy. \tag{30}$$

Since $\int_0^1 \psi_0(y)[u(y) - V_e]\,dy = 0$, any particular solution of Eq. (26), independently of the additive constant C, will provide the same value of ε_e.

It is rather straightforward to prove (see Appendix) that:

$$\int_0^1 \psi_0(y)\,[V_e - u(y)]\,b(y)\,dy = -\varepsilon\int_0^1 \psi_0(y)[\partial_y b(y)]^2\,dy, \tag{31}$$

so

$$\varepsilon_e = \varepsilon + \varepsilon\int_0^1 \psi_0(y)[\partial_y b(y)]^2\,dy \geqslant 0. \tag{32}$$

Inequality (32) indicates that the axial dispersion coefficient D_e is always greater than or at most equal to the diffusion coefficient D (i.e., $\varepsilon_e \geqslant \varepsilon$).

IV. TRANSVERSE DISTRIBUTION

As the transverse motion along y is completely decoupled from axial dynamics, the marginal transverse probability density function $p_y(y,t) = \int_{-\infty}^{\infty} p(x,y,t)\,dx$ satisfies the reduced equation

$$\partial_t\,p_y(y,t) = \mathcal{L}_y[p_y(y,t)], \tag{33}$$

where $\mathcal{L}_y$ is the transverse advection-diffusion operator defined in the previous section and equipped with the boundary conditions $\partial_y\,p_y(y,t)|_{y=0,1} = 0$. The probability density function $p_y(y,t)$ converges towards the stationary equilibrium distribution $\psi_0(y)$, solution of the elliptic problem $\mathcal{L}_y[\psi_0(y)] = 0$, $\partial_y\psi_0(y)|_{y=0,1} = 0$, $\int_0^1 \psi_0(y)\,dy = 1$. Integrating once with respect to y, this equation returns:

$$\varepsilon\,\partial_y\psi_0(y) - \nu\,\sin(2\pi k y)\,\psi_0(y) = C, \tag{34}$$

where the constant C should be vanishing because of the boundary conditions and of the vanishing acoustophoretic force at the walls. Therefore,

$$\psi_0(y) = \frac{1}{Z^{(+)}}\exp\left[-\mathrm{Pe}_\nu\cos(2\pi k y)/2\pi k\right], \tag{35}$$

where $Z^{(+)} = \int_0^1 \exp\left[-\mathrm{Pe}_\nu\cos(2\pi k y)/2\pi k\right]dy$ and $\mathrm{Pe}_\nu = \nu/\varepsilon = \nu\mathrm{Pe}$. In the expression of the transverse equilibrium distribution, the acoustophoretic intensity ν can be rescaled into an effective Peclét number Pe_ν [32].

For large $\mathrm{Pe}_\nu \geqslant 10$, the Frobenius distribution can be approximated by means of Gaussian functions. The distribution $\psi_0(y)$ becomes progressively (as Pe_ν increases) localized at the local minima (stable nodes) $y^*_{n,k}$ of the potential $\cos(2\pi k y)$, where

$$y^*_{n,k} = \frac{1+2n}{2k}, \quad n = 0,\ldots,k-1. \tag{36}$$

Expanding the acoustophoretic potential up to the second order around each $y^*_{n,k}$, $\cos(2\pi k y) = -1 + 4\pi^2 k^2 (y - y^*_{n,k})^2 + \mathcal{O}[(y - y^*_{n,k})^4]$, the transverse equilibrium distribution can be approximated by the equation:

$$\psi_0(y) = \sqrt{\frac{\mathrm{Pe}_\nu}{k}}\sum_{n=0}^{k-1} e^{-\beta(y - y^*_{n,k})^2}, \tag{37}$$

where $\beta = \pi\mathrm{Pe}_\nu k$. Figure 2 depicts the stationary Frobenius distribution for $k = 1$ and $k = 3$ compared with the results of numerical simulations of the Langevin equations of motion (7) at time $t = 20$, obtained from an ensemble of 10^5 particles initially located at $x = 0$, $y = y_c = 1/3$.

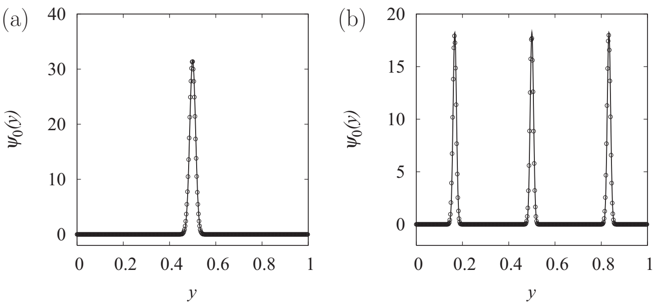

FIG. 2. Stationary transverse distribution $\psi_0(y)$ vs y at $\mathrm{Pe}_\nu = 10^3$ for two different values of k. Solid lines represent Eq. (37), and symbols ($\circ$) are the results of Langevin simulations. (a) $k = 1$; (b) $k = 3$.

The equilibrium distribution becomes localized in a Gaussian way around the stable nodes $y^*_{n,k}$ of the acoustophoretic force, with a square variance (around each node) equal to

$$\sigma_y^2 = \frac{1}{2\beta} = \frac{1}{2\pi \mathrm{Pe}\nu k}. \tag{38}$$

Given the Frobenius distribution $\psi_0(y)$, it is possible to obtain the estimate of the effective axial velocity V_e through Eq. (23). For $\mathrm{Pe}_\nu \to \infty$, the effective axial velocity converges towards the asymptotic value $V_e^* = k^{-1}\sum_{n=0}^{k-1} u(y^*_{n,k})$ corresponding to the arithmetic average of $u(y)$ sampled at the stable nodes: $V_e^* = 1.5$ at $k = 1$, $V_e^* = 1.125$ at $k = 2$, and $V_e^* = 1.05555556$ at $k = 3$. Figure 3(a) depicts the comparison of $V_e^* - V_e$ as a function of the rescaled Peclét number Pe_ν obtained from Langevin simulations of stochastic particle dynamics and the theoretical prediction of homogenization analysis Eq. (23) where the expression (35) for the Frobenius distribution has been used. In point of fact, using the Gaussian representation (37) it is possible to obtain an analytic approximation of V_e that applies for high values of Pe_ν. Inserting Eq. (37) into Eq. (23), and developing the relatively tedious quadrature involved, one finally obtains:

$$V_e = \frac{6}{k\sqrt{\pi}} \sum_{n=0}^{k-1} \Bigg[\left[y^*_{n,k} - (y^*_{n,k})^2 \right] I_1(n) + \frac{1 - 2y^*_{n,k}}{2\sqrt{\beta}}\, I_2(n) - \frac{1}{\beta}\, I_3(n) \Bigg], \tag{39}$$

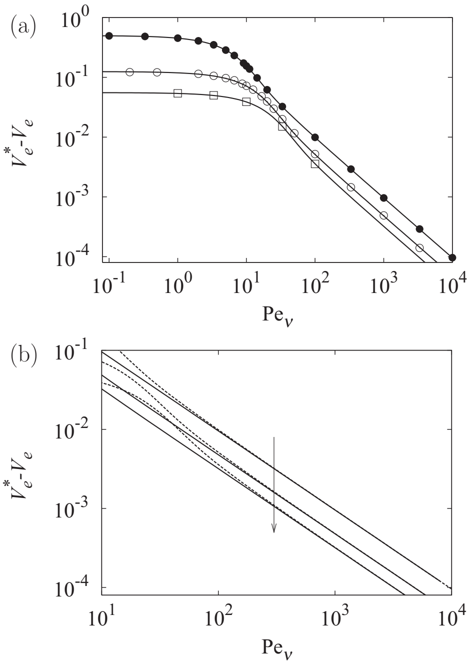

FIG. 3. $V_e^* - V_e$ vs the effective Peclét number Pe_ν for different values of $k = 1,2,3$. Symbols in (a) refer to Langevin simulations: (●) $k = 1$, (○) $k = 2$, (□) $k = 3$. The solid lines in (a) correspond to the theoretical prediction in Eq. (23). (b) Comparison of the theoretical prediction (dashed lines) with the Gaussian approximation (39) and (40) for the effective velocity (solid lines). The arrow indicates increasing values of $k = 1,2,3$.

where

$$\begin{aligned} I_1(n) &= \frac{\sqrt{\pi}}{2}[\mathrm{erf}[\sqrt{\beta}(1 - y^*_{n,k})] + \mathrm{erf}(\sqrt{\beta}\, y^*_{n,k})] \\ I_2(n) &= e^{-\beta(y^*_{n,k})^2} - e^{-\beta(1-y^*_{n,k})^2} \\ I_3(n) &= -\frac{\sqrt{\beta}}{2}[y^*_{n,k} e^{-\beta(y^*_{n,k})^2} + (1 - y^*_{n,k}) e^{-\beta(1-y^*_{n,k})^2}] + \frac{1}{2} I_1(n). \end{aligned} \tag{40}$$

Figure 3(b) depicts the comparison of the Gaussian approximation Eqs. (39) and (40) against the theoretical expression. The Gaussian approximation is extremely accurate starting from $\mathrm{Pe}_\nu \geqslant 10^2$. From scaling analysis it follows that $|V_e^* - V_e| \sim \mathcal{O}(\varepsilon) = \mathcal{O}(\mathrm{Pe}_\nu^{-1})$.

It can be observed in Fig. 3(a) that the Langevin simulations for $k = 3$ are limited to values of Pe_ν of order 10^2. These simulations have been obtained starting from an initial particle distribution localized at $x = 0$ and $y = y_c = 1/3$. Indeed, for $k = 3$, the relaxation dynamics towards the stationary distribution is extremely slow (for generic initial conditions) as thoroughly discussed in the next two sections.

V. AXIAL DISPERSION REGIMES

This section analyzes long-term or large-distance dispersion properties along the axial coordinate deriving from the interplay between the axial velocity field [that we assume to be of Poiseuille type $u(y) = 6(y - y^2)$] and the transverse acoustophoretic potential.

Three different dispersion regimes can be observed, referred to as Case-I, Case-II, and Case-III dispersion, respectively, depending on the structure and location of the stable nodes $\{y^*_{n,k}\}_{n=0}^{k-1}$ of the acoustophoretic potential with respect to the shape of the axial velocity profile.

The analysis is organized as follows. The first paragraph discusses the spectral solution of Eq. (26) for the b field, controlling the value of the effective dispersion coefficient through Eqs. (30) or (32).

The physical conditions under which each of these three regimes can be observed are developed in paragraph V B. The theoretical expression (30) deriving from moment analysis is compared with numerical results obtained from the numerical solution of the Langevin equation of motion (7). Paragraph V C develops a theoretical analysis of the b-field equation aimed at predicting the occurrence and the properties of these three dispersion regimes.

Finally, paragraph V D completes the picture, discussing the influence of the intensity ν of the acoustophoretic potential on dispersion properties.

A. *b*-field equation: Numerical spectral analysis

The equation for the b-field (26) can be solved using Fourier methods. Let $r(y) = \psi_0(y)b(y)$, so Eq. (26) can be rewritten as $\mathcal{L}_y[r(y)] = \psi_0(y)[V_e - u(y)]$. Because of the boundary conditions $\partial_y r(y)|_{y=0,1} = 0$, $r(y)$ can be expanded in cosine-Fourier series,

$$r(y) = \sum_{n=0}^{N} r_n \cos(n\pi y), \tag{41}$$

truncated up to a given order N. In this way, Eq. (26) becomes a linear system in the Fourier coefficients of $r(y)$:

$$\sum_{m=0}^{N} L_{m,n}\, r_n = F_m\,, \quad n = 0,1,\ldots,N, \tag{42}$$

where:

$$\begin{aligned} L_{m,n} &= -\varepsilon(m\pi)^2\delta_{m,n} + \nu D_{m,n},\\ D_{m,n} &= -\frac{m\pi}{\sigma_m^2}\, CSS(n,m,2k), \end{aligned} \tag{43}$$

where $\delta_{m,n}$ are the Kronecker symbols, $\sigma_0^2 = 1$, $\sigma_m^2 = 1/2$, $m = 1,2,\ldots$, and

$$\begin{aligned} CSS(n,m,q) &= \int_0^1 \cos(n\pi y)\,\sin(m\pi y)\,\sin(q\pi y)\,dy\\ &= \frac{\sigma_n^2}{2}[\widehat{\delta}_{n,m-q} - \widehat{\delta}_{n,m+q}], \end{aligned} \tag{44}$$

where $\widehat{\delta}_{n,m}$ are the extended Kronecker symbols, $\widehat{\delta}_{m,n} = 1$, if $|n| = |m|$ and $\widehat{\delta}_{m,n} = 0$ otherwise. Given the cosine-Fourier representation of the stationary Frobenius distribution $\psi_0(y) = \sum_{n=0}^{\infty}\psi_{0,n}\cos(n\pi y)$, the forcing term F_m entering Eq. (42) can be expressed as:

$$F_m = \frac{1}{\sigma_m^2}\sum_{n=0}^{N} G_{m,n}\psi_{0,n}, \quad m = 0,1,\ldots,N, \tag{45}$$

where:

$$\begin{aligned} G_{m,n} = \tfrac{1}{2}\big[&V_e\big(C_{m+n}^{(0)} + C_{m-n}^{(0)}\big) - 6\big(C_{m+n}^{(1)} + C_{m-n}^{(1)}\\ &- C_{m+n}^{(2)} - C_{m-n}^{(2)}\big)\big], \end{aligned} \tag{46}$$

and $C_n^{(h)} = \int_0^1 y^h\cos(n\pi y)\,dy$, $h = 0,1,2$, $n \in \mathbf{N}$. Equation (42) can be represented in matrix form as $\mathbf{L}\,\mathbf{r} = \mathbf{F}$, where $\mathbf{r} = (r_0,\ldots,r_N)^t$, $\mathbf{F} = (F_0,\ldots,F_N)^t$, and $\mathbf{L} = (L_{m,n})_{m,n=0}^N$. Since the matrix $\mathbf{L}$ is singular—due to the fact that the corresponding operator $\mathcal{L}_y$ admits a conservation eigenvalues $\lambda_0 = 0$ and, consequently, the linear system (26) possesses an uncountable set of solutions differing from each other by an additive constant—a solution of Eq. (42) can be obtained by solving the equivalent system

$$\widehat{\mathbf{L}}\,\mathbf{r} = \mathbf{F}, \tag{47}$$

where

$$\widehat{L}_{m,n} = L_{m,n} + \delta_{0,0}, \quad m,n = 0,\ldots,N. \tag{48}$$

The choice of the truncation order N in the Fourier expansion depends on the Peclét number. We use $N = 400$ for low Pe values (usually $\leqslant 10^2$) up to $N = 4\times10^3$ for higher values (up to Pe $= 10^6$).

Let us express the reciprocal of the dispersion Peclét number as $\varepsilon_e = \varepsilon + \varepsilon_{\text{conv}}$, i.e., as the combination of two contributions: ε deriving from axial diffusion and $\varepsilon_{\text{conv}}$ representing the convection-enhancement induced by the interplay among axial velocity, acoustophoretic potential, and thermal fluctuations. Given the Fourier representation of $r(y)$, the term $\varepsilon_{\text{conv}}$ can be expressed as:

$$\begin{aligned} \varepsilon_{\text{conv}} &= \int_0^1 r(y)\,[u(y) - V_e]\,dy\\ &= \sum_{n=0}^{N} r_n\big[6C_n^{(1)} - 6C_n^{(2)} - V_e C_n^{(0)}\big]. \end{aligned} \tag{49}$$

As moment predictions are validated in the next paragraph against numerical simulations of stochastic particle dynamics, let us briefly summarize the setup for these simulations. Equations (7) are simulated numerically using the classical Euler-Langevin algorithm, with a time step of $h_t = 2\times10^{-3}$. As ensemble of N_p particles $\{(x^{(h)},y^{(h)})\}_{h=1}^{N_p}$ is considered with $N_p = 10^5$ up to $N_p = 10^6$, depending on the simulations. The initial conditions $\{(x_0^{(h)},y_0^{(h)})\}_{h=1}^{N_p}$ at $t = 0$ are localized at the "inlet section" $x = 0$, i.e., $x_0^{(h)} = 0$, $h = 1,\ldots,N_p$, while for the transverse coordinate several configurations are considered: either localized at a single point, i.e., $y_0^{(h)} = y_c$, $h = 1,\ldots,N_p$, or considering $\{y_0^{(h)}\}_{h=1}^{N_p}$ uniformly distributed through the transverse section. The choice of the initial particle distribution does not influence the estimate of the asymptotic transport properties but has a deep impact on transient dispersion properties as addressed in Sec. VI.

B. Dispersion regimes

For the transport problem under investigation, three different dispersion regimes can be identified that correspond to three qualitatively different asymptotic behaviors of ε_e vs Pe for large Peclét numbers. Throughout this subsection we consider the normalized case $\nu = 1$ and use the notation $s(y) = \nu\sin(2\pi ky)$ to indicate the acoustophoretic force. The influence of ν is discussed in subsections V C and V D.

The first regime, referred to as *Case-I dispersion*, occurs whenever the values of the axial velocity are the same at all the stable nodes $\{y_{n,k}\}_{n=0}^{k-1}$ and the velocity $u(y)$ in the neighborhood of every $y_{n,k}^*$ is at least locally quadratic. Therefore, the two analytic conditions defining Case-I dispersion are (i) $u(y_{n,k}^*) = u^*$, $\forall n = 0,\ldots,k-1$ and (ii) $\partial_y u(y)|_{y=y_{n,k}^*} = 0$, $\forall n = 0,\ldots,k-1$.

The prototype of this situation is represented by an acoustophoretic contribution $s(y) = \sin(2\pi y)$, i.e., $k = 1$, since there exists a single stable node exactly at the abscissa of the local maximum of the Poiseuille profile $u(y)$ (channel midpoint $y_{0,1}^* = 1/2$), as depicted in Fig. 4(a).

Axial dispersion in this case can be viewed as a constrained Taylor-Aris dispersion in which the acoustophoretic potential near the stable nodes shrinks the spatial range of influence (represented by the transverse variance σ_y) of Brownian fluctuations. This constraint is progressively more effective for increasing Pe values and annihilates the fluctuations for Pe $\to\infty$ since $\lim_{\text{Pe}\to\infty}\sigma_y^2 = 0$.

Since the axial velocity profile is at least locally quadratic near each $y_{n,k}^*$, Brownian particles experience an axial velocity in the neighborhood of each stable node as it would be locally uniform. As for uniform parallel flows (plug flows), Taylor-Aris dispersion theory predicts $\varepsilon_{\text{conv}} = 0$, it is expected that $\varepsilon_{\text{conv}} \to 0$ as Pe diverges.

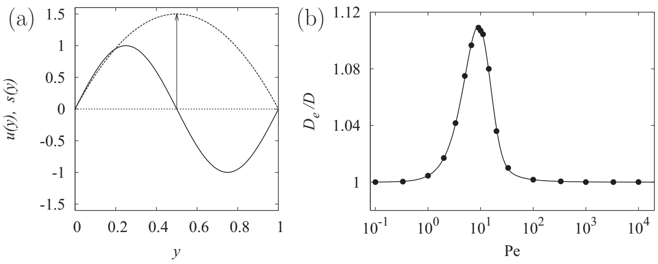

FIG. 4. (a) Schematic representation of the physical conditions giving rise to Case-I dispersion, occurring for $k = 1$. (b) D_e/D vs Pe (at $\nu = 1$) for $k = 1$. Solid line represents the moment prediction, and symbols (●) are the results of Langevin simulations.

Therefore, if one considers the ratio of the effective dispersion coefficient D_e to the diffusivity D,

$$\frac{D_e}{D} = \frac{\varepsilon_e}{\varepsilon} = 1 + \frac{\varepsilon_{\mathrm{conv}}}{\varepsilon}, \tag{50}$$

we expect from physical reasons that $D_e/D \rightarrow 1$ both for very small and very large Pe. For intermediate Pe values, since $\varepsilon_e \geqslant \varepsilon$, the graph of D_e/D should display a unimodal behavior with a local maximum at some Pe value. This qualitative picture justifies the numerical results reported in Fig. 4(b) obtained via Langevin simulations (symbols ●), quantitatively confirmed by moment analysis (solid line).

To sum up, Case-I dispersion is characterized by the the following asymptotic property:

$$\lim_{\mathrm{Pe}\rightarrow\infty} \frac{D_e}{D} = 1, \quad \text{i.e.,} \quad \lim_{\mathrm{Pe}\rightarrow\infty} \varepsilon_{\mathrm{conv}} = 0. \tag{51}$$

Case-II dispersion displays some analogies with respect to Case I, namely the axial velocity profile at all of the stable nodal points attains the same value. Conversely, for Case II no conditions are set on the derivatives of $u(y)$ at $\{y^*_{n,k}\}_{n=0}^{k-1}$. Consequently, the axial velocity in the neighborhood of the stable nodes behaves generically as a shear flow.

The analytical conditions defining the occurrence of Case-II dispersion are (i) $u(y^*_{n,k}) = u^*$, $\forall n = 0,\ldots,k-1$, and (ii) $Du_{\max} = \max_{n=0,\ldots,k-1} |\partial_y u(y)|_{y=y^*_{n,k}} > 0$.

Condition (ii) ensures that there exists at least one stable node at which $\partial_y u(y)$ strictly differs from zero (local shear-flow behavior).

For Poiseuille profiles $u(y)$, a typical situation that satisfies the conditions of Case-II dispersion occurs for $k = 2$, as depicted in Fig. 5(a). Observe that also the case $k = -1$, depicted in Fig. 5(b) falls in this class of dispersion problems.

As for Case I, axial dispersion develops as a constrained Taylor-Aris problem, in which Brownian particles experience, at least at some stable node of the potential, a local shear flow, while the spatial range of influence of velocity nonuniformities shrinks progressively as Pe $\rightarrow \infty$.

This observation suggests that Case-II dispersion should be characterized by a behavior of the ratio D_e/D vs Pe that is "intermediate" between the Taylor-Aris divergence and the collapse of D_e towards D observed for Case I. The typical dispersion patterns in Case II are depicted in Fig. 6.

As can be observed, the ratio D_e/D admits a local maximum for intermediate values of the Peclét number, while it converges for Pe $\rightarrow \infty$ towards a limiting value that is definitely greater than 1. A theoretical and quantitative explanation of this phenomenon is developed in the next paragraph based on the properties of the b-field in the neighborhood of the stable nodes.

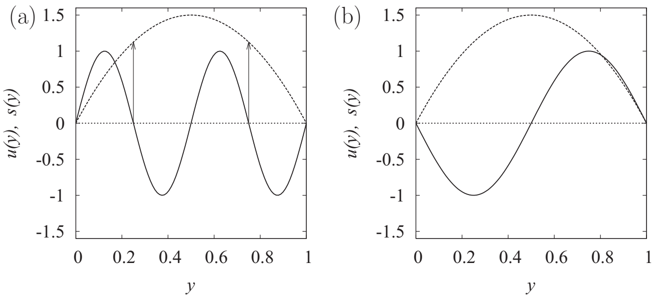

FIG. 5. Schematic representation of the physical conditions originating Case-II dispersion, occurring for $k = 2$ (a) and $k = -1$ (b).

To sum up, the qualitative property characterizing Case-II dispersion is therefore:

$$\lim_{\mathrm{Pe}\rightarrow\infty} \frac{D_e}{D} = \kappa_D > 1, \quad \text{i.e.,} \quad \lim_{\mathrm{Pe}\rightarrow\infty} \varepsilon_{\mathrm{conv}} = \varepsilon^{\infty}_{\mathrm{conv}} > 0. \tag{52}$$

Finally, let us consider the generic situation in the presence of multiple stable nodes, namely that the axial velocities at the stable nodes differ from each other. This condition is referred to as *Case-III dispersion*. Mathematically, Case-III dispersion can be defined by the following conditions: (i) $k > 1$ and (ii) $\Delta u^*_{\max} = \max_{m,n=0,\ldots,k-1} |u(y^*_{n,k}) - u(y^*_{m,k})| > 0$.

The simplest model accounting for these conditions occurs for $k = 3$ in a Poiseuille flow (Fig. 7), although for $k \geqslant 3$ all the acoustophoretic potentials meet these conditions.

Figure 8 depicts the behavior of the axial mean-square displacement $\langle (x - \langle x \rangle)^2 \rangle (t)$ as a function of time t at $k = 3$, for three different values of the Peclét number, obtained from Langevin simulations starting from a uniform distribution of the initial transverse positions at the inlet section $x = 0$. A slight increase in Pe, from Pe $= 60$ to Pe $= 70$ and Pe $= 100$ determines a huge increase of the axial dispersion.

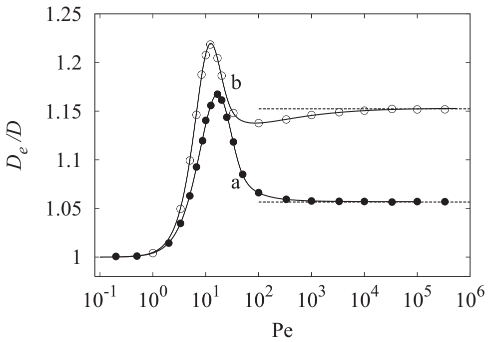

FIG. 6. D_e/D vs Pe for Case-II dispersion. Solid lines represent moment predictions, and symbols (● and ○) denote Langevin simulation results. Line (a) and (●): $k = 2$; line (b) and (○): $k = -1$. Horizontal dotted lines correspond to the limit values for Pe $\rightarrow \infty$.

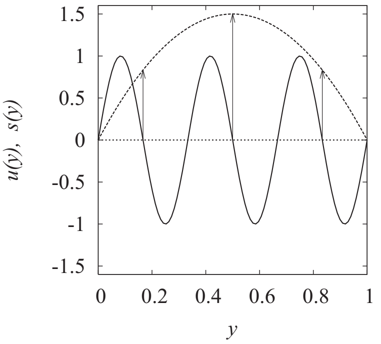

FIG. 7. Schematic representation of the physical conditions giving rise to Case-III dispersion for $k = 3$.

The numerical estimate of $\varepsilon_{\text{conv}}$ and of the ratio D_e/D as a function of Pe for $k = 3$ is depicted in Figs. 9(a) and 9(b), respectively. Moment analysis and Langevin simulations are in excellent agreement with each other and indicate that:

$$\varepsilon_{\text{conv}} \sim \frac{D_e}{D} \sim C\, e^{\mu_k \text{Pe}}, \quad \text{for Pe} \gg 1, \tag{53}$$

where C is a positive constant and $\mu_k > 0$, i.e., the axial dispersion coefficient D_e scales exponentially with the Peclét number. The scaling relation (53) represents the signature of Case-III dispersion.

This is the first physical example, to the best of our knowledge, where an exponential increase of the dispersion coefficient with the Peclét number has been reported and predicted. This phenomenon is a consequence of the fact that the velocity experienced by Brownian particles in the channel $\mathbf{v} = [s(y), u(y)]$ consists of the superposition of a solenoidal axial component $u(y)$ and of a potential one $s(y)$. The exponential divergence of $\varepsilon_{\text{conv}}$ is peculiar of this interplay, since it can be observed neither in purely solenoidal fields nor in purely potential (irrotational) ones. The theoretical explanation of the exponential scaling (53) observed in Case-III dispersion, as well as the prediction of the exponent μ_k, is developed in next paragraph by re-elaborating the b-field equation (26).

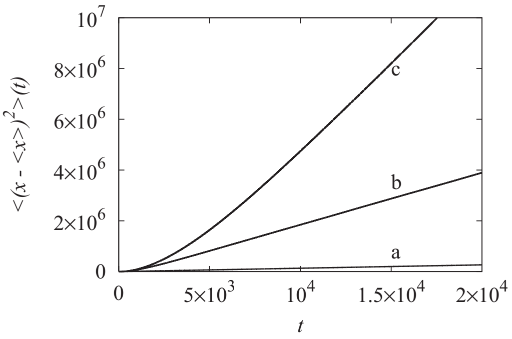

FIG. 8. Axial mean-square displacement $\langle (x - \langle x \rangle)^2 \rangle (t)$ vs time t at $k = 3$, $\nu = 1$ (Case-III dispersion regime) for three different values of the Peclét number. Line (a): $\varepsilon = 1.66 \times 10^{-2}$, Pe $= 60$; line (b): $\varepsilon = 1.143 \times 10^{-2}$, Pe $= 70$; line (c) $\varepsilon = 10^{-1}$, Pe $= 10^2$.

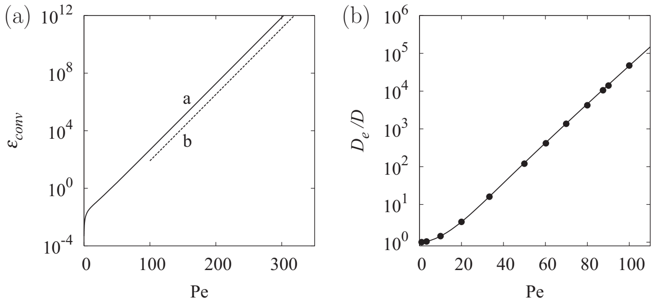

FIG. 9. (a) $\varepsilon_{\text{conv}}$ vs Pe for $k = 3$ ($\nu = 1$) obtained from moment analysis (solid line a). Dashed line (b) represents the theoretical exponential scaling $\varepsilon_{\text{conv}} \sim e^{\text{Pe}/3\pi}$, see Eq. (80) in subsection V C. (b) D_e/D vs Pe: comparison of the prediction of moment theory (line) with the results of Langevin simulations (symbols ●).

C. *b*-field equation: Theoretical analysis

The starting point for a theoretical investigation of the dispersion regimes phenomenologically described in the previous paragraph is the b-field equation (26), controlling via Eqs. (30) or (32) the behavior of ε_e. For notational simplicity set $s(y) = \nu \sin(2\pi k y)$.

Expanding the expression for $\mathcal{L}_y[\psi_0(y)\, b(y)]$, enforcing the fact that the Frobenius distribution satisfies the homogeneous equation $\mathcal{L}_y[\psi_0(y)] = 0$, Eq. (26) can be rewritten in the form:

$$\begin{aligned} -s(y)\, \partial_y b(y) &+ 2\varepsilon[\partial_y \log \psi_0(y)]\, \partial_y b(y) \\ &+ \varepsilon\, \partial_y^2 b(y) = V_e - u(y). \end{aligned} \tag{54}$$

Because of the boundary conditions, and of the fact that $s(y)$ vanishes at $y = 0,1$, equation $\mathcal{L}_y[\psi_0(y)] = 0$ implies

$$-s(y)\, \psi_0(y) + \varepsilon\, \partial_y \psi_0(y) = 0, \tag{55}$$

thus,

$$\varepsilon[\partial_y \log \psi_0(y)] = s(y). \tag{56}$$

Substituting this expression into Eq. (54) one obtain for $b(y)$ the simpler equation

$$s(y)\, \partial_y b(y) + \varepsilon\, \partial_y^2 b(y) = V_e - u(y), \tag{57}$$

that can be easily solved by quadrature by setting $g(y) = \partial_y b(y)$, obtaining a first-order equation for $g(y)$,

$$\varepsilon\, \partial_y g(y) + s(y)\, g(y) = V_e - u(y), \tag{58}$$

subjected to the boundary constraints $g(y)|_{y=0,1} = 0$.

In point of fact, the functional structure of Eq. (58) is fully sufficient to achieve a qualitative theoretical explanation of the dispersive behavior in two of the three regimes without solving explicitly this equation.

First, consider Case-I dispersion, taking $k = 1$ as the paradigmatic prototype of this regime. Set $y^* = y^*_{0,1} = 1/2$. Figure 10(a) shows the behavior of the function $r(y) = \psi_0(y)\, b(y)$ solution of the b-field equation for two values of Pe. As Pe increases, $r(y)$ localizes in the neighborhood of the stable node y^*.

Since $\varepsilon_{\text{conv}} = \int_0^1 r(y)\, [u(y) - V_e]\, dy$, the behavior of $r(y)$ or of $b(y)$ in the neighborhood of y^* controls the properties of $\varepsilon_{\text{conv}}$ for high Peclét values.

Let $u^* = u(y^*)$. Since $u(y)$ is locally quadratic, by condition (ii) defining the Case-I regime in the previous paragraph, we can set, in general,

$$u(y) = u^* + \frac{u''(y^*)}{2}(y - y^*)^2 + \mathcal{O}[(y - y^*)^3]. \tag{59}$$

Moreover,

$$V_e = u^* + \mathcal{O}(\varepsilon) \tag{60}$$

and

$$s(y) = s'(y^*)(y - y^*) + \mathcal{O}[(y - y^*)^2]. \tag{61}$$

As y^* is an internal point in (0,1), $\varepsilon \partial_y g(y) \sim \mathcal{O}(\varepsilon)$ and the solution of Eq. (58) in the neighborhood of y^* can be expressed as:

$$g(y) = \frac{V_e - u(y)}{s(y)} + \mathcal{O}(\varepsilon) = -\frac{u''(y^*)}{2\,s'(y^*)}(y - y^*) + \mathcal{O}(\varepsilon). \tag{62}$$

As a consequence, the field $b(y)$ behaves quadratically in the neighborhood of y^*:

$$b(y) = -\frac{u''(y^*)}{4\,s'(y^*)}(y - y^*)^2 + C, \tag{63}$$

where C is some immaterial additive constant. In the case $k = 1$ for the Poiseuille profile, $u''(y^*) = -12$, $s'(y^*) = -2\pi\nu$, and Eq. (63) becomes

$$b(y) = -\frac{3}{2\pi\nu}(y - y^*)^2 + C\,. \tag{64}$$

Figure 10(b) compares the theoretical prediction (64) with the $b(y)$ profile obtained by the direct solution of Eq. (26) using spectral methods. The agreement is excellent.

For large Pe values we can use Eq. (64) to predict the behavior of the effective dispersion coefficient. From Eq. (32), substituting the expression (62) for $g(y)$ and the Gaussian approximation (37) for $\psi_0(y)$, one obtains for the Poiseuille flow:

$$\varepsilon_e = \varepsilon + \varepsilon\left(\frac{9}{\pi^2\nu^2}\right)\underbrace{\sqrt{\mathrm{Pe}\nu}\int_0^1 (y - y^*)^2 e^{-\beta(y-y^*)^2}\,dy}_{\sigma_y^2}\,. \tag{65}$$

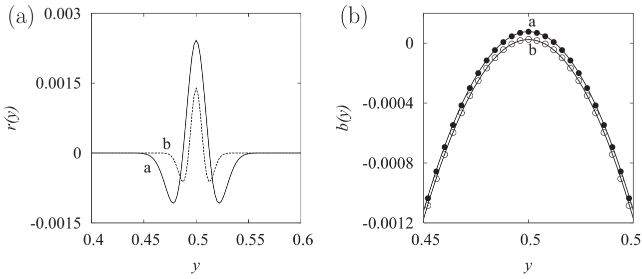

FIG. 10. Case-I dispersion ($k = 1$). (a) $r(y)$ vs y for $\mathrm{Pe} = 10^3$ [solid line (a)], and $\mathrm{Pe} = 3 \times 10^3$ [dashed line (b)]. (b) $b(y)$ vs y in the neighborhood of $y^* = 1/2$. Solid lines represent the theoretical predictions based on Eq. (64) and symbols the results of moment analysis. Line (a) and symbols (●): $\mathrm{Pe} = 10^3$; line (b) and symbols (○): $\mathrm{Pe} = 3 \times 10^3$.

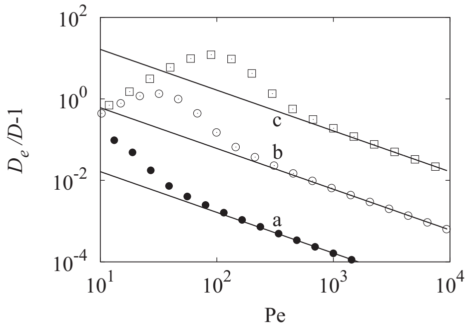

FIG. 11. $D_e/D - 1$ vs Pe for $k = 1$ (Case-I dispersion). Symbols are the results of moment analysis and solid lines the theoretical prediction Eq. (65) valid for large Pe. Line (a) and (○): $\nu = 1$; line (b) and (●): $\nu = 0.3$; line (c) and (□): $\nu = 0.1$.

The integral term entering Eq. (65) is simply the transverse variance σ_y^2 given by Eq. (38). As a consequence, from Eq. (65) we infer the following properties in Case-I dispersion: (i) For large Pe, $\varepsilon_e \to \varepsilon$ and (ii) $\varepsilon_e/\varepsilon - 1 \sim \mathrm{Pe}^{-1}$. Figure 11 depicts the behavior of $D_e/D - 1$ for high Peclét values obtained from Eq. (65) compared with moment-analysis results, confirming the theory.

Case-II dispersion can be treated in a similar way. Figure 12(a) depicts the typical profile of the field $r(y)$ at high Peclét value, showing localization around the stable nodes. Consequently, also in this case, a purely local analysis of the field $b(y)$ is sufficient to predict dispersion properties for high Pe values.

For technical simplicity, consider the case (as for $k = 2$) where the stable nodes fall inside the interval (0,1). Let $u^* = u(y^*_{n,k})$, $n = 0, \ldots, k - 1$, and consider any $y^* = y^*_{n,k}$ (for fixed n) stable node of the acoustophoretic potential. In the neighborhood of y^*, we have for large Pe:

$$u(y) = u^* + u'(y^*)(y - y^*) + \mathcal{O}[(y - y^*)^2], \tag{66}$$

while Eqs. (60) and (61) apply also in this case for V_e and $s(y)$, respectively. For any internal y^*, $\varepsilon(\partial_y g) \sim \mathcal{O}(\varepsilon)$, and, consequently, in the neighborhood of y^*,

$$g(y) = -\frac{u'(y^*)}{s'(y^*)} + \mathcal{O}(\varepsilon). \tag{67}$$

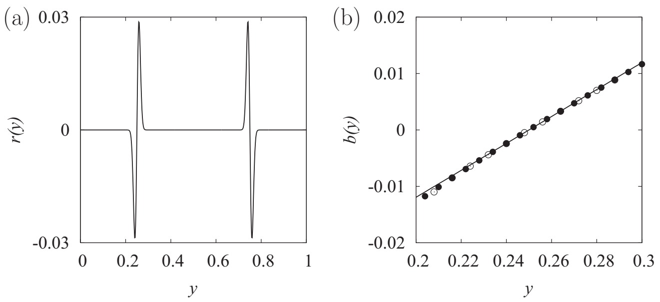

FIG. 12. Case-II dispersion ($k = 2$). (a) $r(y)$ vs y for $\mathrm{Pe} = 10^3$. (b) $b(y)$ vs y in the neighborhood of $y^*_{0,2} = 1/4$. Solid line represents the theoretical prediction based on Eq. (68) and the symbols the results of moment analysis: (●) $\mathrm{Pe} = 10^3$; (○) $\mathrm{Pe} = 3 \times 10^3$.

It follows from Eq. (67) that $b(y)$ is locally linear,

$$b(y) = -\frac{u'(y^*)}{s'(y^*)}(y - y^*) + C, \tag{68}$$

where the value of the additive constant C is physically immaterial. Figure 12(b) compares this result with spectral simulations of the field $b(y)$ for $k = 2$ in the neighborhood of $y^* = 1/4$.

Obviously Eq. (67) applies to each $y^*_{n,k}$, so $g(y) = -[u'(y^*_{n,k})/s'(y^*_{n,k})] + \mathcal{O}(\varepsilon)$ in the neighborhood of each stable node $y^*_{n,k}$. In the symmetric case where all the factors $[u'(y^*_{n,k})/s'(y^*_{n,k})]$ are equal for $n = 0,\ldots,k-1$ one obtains a particularly simple expression for the dispersion coefficient. This is the case of $k = 2$ in the presence of a Poiseuille flow. From Eq. (67) the following asymptotic value of the axial dispersion coefficient can be inferred:

$$\varepsilon_e = \varepsilon + \varepsilon \int_0^1 \psi_0(y) g^2(y)\, dy = \varepsilon + \varepsilon \left[\frac{u'(y^*)}{s'(y^*)}\right]^2. \tag{69}$$

This theoretical argument shows that for Case-II dispersion the ratio $\varepsilon_e/\varepsilon$ remains bounded and converges for Pe → ∞ to a limit value that is strictly greater than 1. In the symmetric case where Eq. (69) applies, this limit value equals $1 + [u'(y^*)/s'(y^*)]^2$. For instance, in the case of a Poiseuille flow profile at $k = 2$, $y^* = 1/4, 3/4$, $u'(y^*) = 4$, $s'(y^*) = -4\pi\nu$ so for $\nu = 1$ one obtains:

$$\lim_{\mathrm{Pe}\to\infty} \frac{\varepsilon_e}{\varepsilon} = 1 + \left(\frac{3}{4\pi}\right)^2 = 1.057\ldots, \tag{70}$$

in perfect agreement with the simulation results reported in Fig. 6.

Consider now Case-III dispersion, i.e., whenever there is more than a single stable node and the axial velocities at these nodes different from each other. Let $y^* = y^*_{n,k}$ any of these nodes for a fixed value of the integer $n \leqslant k-1$. Close to y^*, $u(y) = u(y^*) + u'(y^*)(y - y^*)$, but $V_e = u_m + \mathcal{O}(\varepsilon)$, where $u_m = k^{-1}\sum_{n=0}^{k-1} u(y^*_{n,k}) \neq u(y^*)$. Therefore, if one neglects $\varepsilon\partial_y g(y)$ in Eq. (58), one would obtain $g(y) = [V_e - u(y)]/s(y) \to \infty$ for $y \to y^*$. This result is indeed correct in the limit for Pe → ∞, as both $r(y)$ and $b(y)$ diverge at any $y = y^*$ for Pe → ∞ [see Fig. 13(a)]. Nevertheless, in order to obtain an expression for the scaling or $\varepsilon_{\mathrm{conv}}$ with Pe a more refined analysis of Eq. (58) is required.

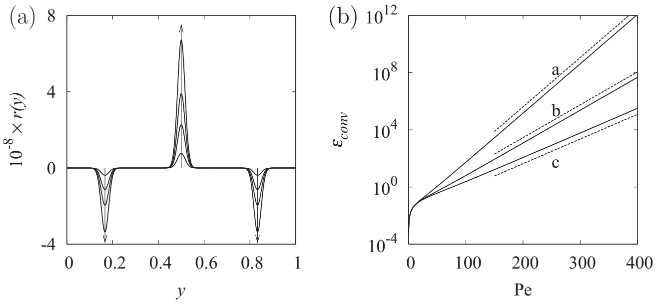

FIG. 13. Case-III dispersion. (a) $10^{-8} \times r(y)$ vs y for $k = 3$. The arrows indicate increasing values of $\mathrm{Pe} = 1.8 \times 10^2, 1.9 \times 10^2, 1.95 \times 10^2, 2 \times 10^{-2}$. (b) $\varepsilon_{\mathrm{conv}}$ vs Pe for different values of k ($k > 3$, $\nu = 1$). Solid lines a: $k = 4$,;b: $k = 6$; and (c) $k = 8$. The corresponding dashed lines represent the theoretical scalings $\varepsilon_{\mathrm{conv}} \sim e^{\mathrm{Pe}/k\pi}$.

The general solution of Eq. (58) is given by:

$$g(y) = e^{-S(y)/\varepsilon}\left\{A + \frac{1}{\varepsilon}\int_0^y [V_e - u(\eta)]\, e^{S(\eta)/\varepsilon}\, d\eta\right\}, \tag{71}$$

where A is an integration constant and $S(y) = \int^y s(\eta)\, d\eta$. Because of the boundary constraint at $y = 0$, $g(0) = 0$ implies $A = 0$ so Eq. (71) becomes:

$$g(y) = \frac{e^{-S(y)/\varepsilon}}{\varepsilon}\int_0^y [V_e - u(\eta)]\, e^{S(\eta)/\varepsilon}\, d\eta\,. \tag{72}$$

Observe that this expression satisfies the other constraint at $y = 1$ identically. This stems from the fact that the Frobenius distribution can be expressed as:

$$\psi_0(y) = e^{S(y)/\varepsilon}/Z^{(+)}, \quad Z^{(+)} = \int_0^1 e^{S(y)/\varepsilon}\, dy, \tag{73}$$

so $g(1) = (Z^{(+)}e^{-S(1)/\varepsilon}/\varepsilon)\int_0^1 [V_e - u(\eta)]\, \psi_0(\eta)\, d\eta = 0$. Using Eq. (73), the function $g(y)$ can be expressed as:

$$g(y) = \frac{1}{\varepsilon\, \psi_0(y)}\int_0^y [V_e - u(\eta)]\, \psi_0(\eta)\, d\eta, \tag{74}$$

so

$$\varepsilon_{\mathrm{conv}} = \frac{1}{\varepsilon^2}\int_0^1 \frac{W^2(y)}{\psi_0(y)}\, dy,$$
$$W(y) = \int_0^y [V_e - u(\eta)]\, \psi_0(\eta)\, d\eta. \tag{75}$$

The function $W(y)$ is a “window” function $W(0) = W(1) = 0$, bounded for any y, and converging for Pe → ∞ towards a piecewise constant function $W_\infty(y)$ [see Figs. 14(a) and 14(b)], given by:

$$W_\infty(y) = \frac{1}{k}\int_0^y [V_e - u(y^*_{n,k})]\delta(\eta - y^*_{n,k})\, d\eta. \tag{76}$$

It follows from Eq. (75) for large Pe,

$$\varepsilon_{\mathrm{conv}} = \frac{1}{\varepsilon^2}\int_0^1 \frac{dy}{\psi_0(y)} \sim \frac{Z^{(+)}Z^{(-)}}{\varepsilon^2}, \tag{77}$$

where $Z^{(-)} = \int_0^1 e^{-S(y)/\varepsilon}\, dy$. The integral $Z^{(-)}$ is analogous to $Z^{(+)}$, but with a reverse potential, making the unstable nodes stable and vice versa. Consequently, both $Z^{(+)}$ and $Z^{(-)}$ possess the same exponential scaling with Pe, controlled by the

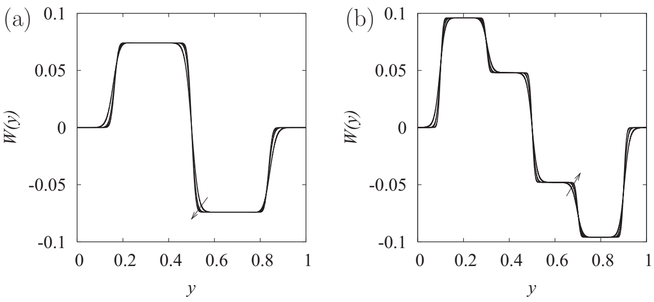

FIG. 14. Case-III: window function $W(y)$ vs y. The arrows indicate increasing values of Pe. (a) $k = 3$, $\mathrm{Pe} = 10^2, 2 \times 10^2, 3 \times 10^2$. (b) $k = 5$, $\mathrm{Pe} = 10^2, 2 \times 10^2, 4 \times 10^2$.

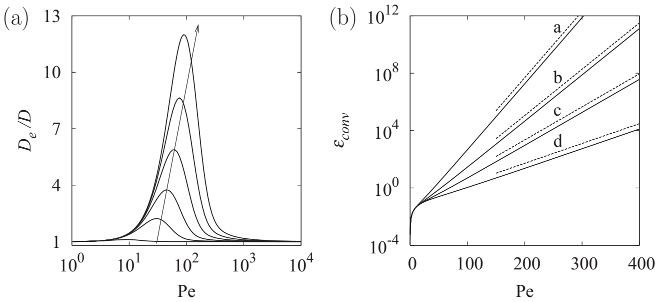

FIG. 15. (a) Case I, D_e/D vs Pe at $k = 1$ for different values of ν. The arrow indicates decreasing values of $\nu = 1, 0.3, 0.2, 0.15, 0.12, 0.1$. (b) Case III, $\varepsilon_{\text{conv}}$ vs Pe at $k = 3$ for different values of ν. Solid lines a: $\nu = 1$; b: $\nu = 0.7$; c: $\nu = 0.5$; and d: $\nu = 0.3$. The corresponding dashed lines represent the theoretical scalings $\varepsilon_{\text{conv}} \sim e^{\text{Pe}\nu/k\pi}$ with the exponent μ_k given by Eq. (80).

value of $e^{S(y)/\varepsilon}$ and $e^{-S(y)/\varepsilon}$ at the unstable and stable nodes, respectively, i.e.,

$$Z^{(-)} \sim Z^{(+)} = \int_0^1 e^{-\text{Pe}\,\nu\cos(2\pi k y)/(2\pi k)}\, dy \sim e^{\text{Pe}\nu/2\pi k}. \tag{78}$$

It follows from Eq. (78) that:

$$\varepsilon_{\text{conv}} \sim \frac{(e^{\text{Pe}\nu/2\pi k})^2}{\varepsilon^2} \sim e^{\text{Pe}\nu/\pi k}, \tag{79}$$

which indicates that the exponent μ_k entering Eq. (53) is given by:

$$\mu_k = \frac{\text{Pe}\,\nu}{\pi\, k}. \tag{80}$$

The theoretical prediction expressed by Eq. (80) is in perfect agreement with the numerical data depicted in Fig. 9(a) for $k = 3$ and in Fig. 13 for $k > 3$.

D. Influence of the acoustophoretic intensity ν

Particle motion in the overdamped regime Eq. (7) depends on two parameters: the particle Peclét number and the dimensionless acoustophoretic intensity ν. In this paragraph we address succinctly the influence of the latter.

There are two contrasting effects of ν on dispersion, occurring for Cases I and II and for Case III, respectively. In Cases I and II, lower values of ν determine higher values of the ratio D_e/D for intermediate Peclét numbers (Pe > 1). Moreover, in Case II, an asymptotic higher values of the limit ratio κ_D can be observed and reported in Figs. 15(a) and 16(a). This is a consequence of the fact that that as ν decreases, Taylor-Aris dispersion [i.e., $D_e = D + V^2H^2\Gamma_{\text{TA}}/D$, where Γ_{TA} is the Taylor-Aris coefficient and $\Gamma_{\text{TA}} = 1/105$ in two-dimensional (2D) Poiseuille flow], that is controlled exclusively by the solenoidal axial velocity, becomes more pronounced at intermediate Peclét values.

Specifically, the local theory developed in the previous paragraph provides the expression for the limit value of $\varepsilon_e/\varepsilon$ in Case-II dispersion ($k = 2$):

$$\lim_{\text{Pe}\to\infty} \frac{\varepsilon_e}{\varepsilon} = \kappa_D = 1 + \left(\frac{3}{4\pi\,\nu}\right)^2, \tag{81}$$

in perfect agreement with numerical analysis [Fig. 16(b)].

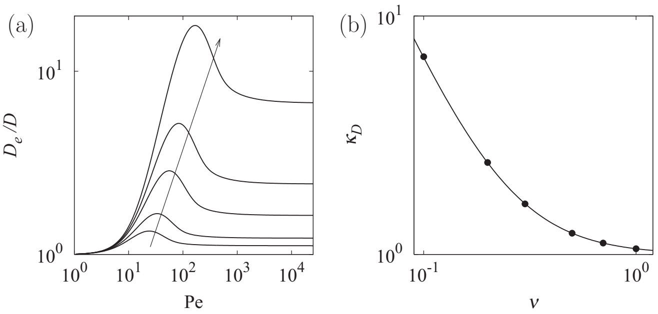

FIG. 16. Case-II dispersion ($k = 2$). (a) D_e/D vs Pe for different values of ν. The arrow indicates decreasing values of $\nu = 0.7, 0.5, 0.3, 0.2, 0.1$. (b) Limit value κ_D vs ν. Symbols (●) represent the numerical estimate based on the data reported in panel (a), and the solid line the theoretical prediction Eq. (81).

Conversely, the amplitudes of the potential barriers between neighboring stable nodes, which control the exponential scaling characterizing Case-III dispersion Eq. (79), decrease with ν as predicted by Eq. (80) and confirmed numerically [Fig. 15(b)].

VI. ANOMALOUS TRANSIENT AXIAL DISPERSION

The presence of different axial velocities at the stable nodal points, which represents the main signature of Case-III dispersion, implies an interesting short or intermediate term dispersive dynamics. In point of fact, the occurrence of exponentially high values of the dispersion coefficient with Pe is related one to one with the extremely slow relaxation of the marginal axial distribution $p_x(x,t) = \int_0^1 p(x,y,t)\,dy$ towards the equilibrium Frobenius eigenfunction $\psi_0(y)$ that controls the onset of the long-term or large-distance transport described by the effective transport parameters V_e and D_e Eq. (10). This implies, in passing, that the transient properties and not the long-term dynamics are the crucial dispersive features controlling the design and optimization of practical acoustophoretic microflow devices in Case-III conditions.

Figure 17 depicts the typical axial dynamics in Case-III dispersion. This figure shows the temporal behavior of the

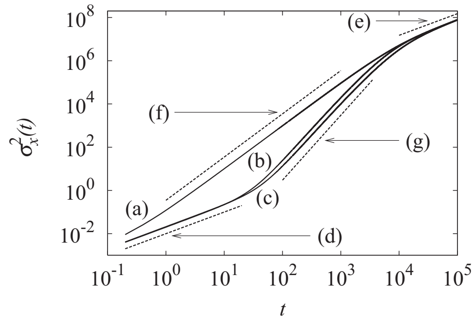

FIG. 17. $\sigma_x^2(t)$ vs t for $k = 3$, $\nu = 1$, $\varepsilon = 10^{-2}$. Solid lines reproduce the results of Langevin simulations: starting from a uniform initial transverse distribution [line (a)], a localized transverse distribution at $y_c = 1/2$ [line (b)], a localized transverse distribution at $y_c = 0.2$ [line (c)]. Dashed lines represent the scalings $\sigma_x^2(t) \sim t$ [lines (d) and (e)], $\sigma_x^2(t) \sim t^2$ [line (f)], and $\sigma_x^2(t) \sim t^3$ [line (g)].

mean-square axial displacement $\sigma_x^2(t) = \langle (x - \langle x \rangle)^2 \rangle (t)$ in Case-III conditions ($k = 3$, $\nu = 1$) obtained from Langevin simulations considering $N_p = 10^6$ particles. Several different initial conditions are considered, belonging to two classes of inlet transverse distributions: (i) $x^{(h)} = 0$ and the $y^{(h)}$'s, $h = 1,\ldots,N_p$, uniformly distributed throughout the cross section (referred to as U conditions); (ii) $x^{(h)} = 0$ and $y^{(h)} = y_c$, $h = 1,\ldots,N_p$, i.e., all the particles of the ensemble are injected at the same transversal location y_c, thus $p_y(y,0) = \delta(y - y_c)$ (referred to as L conditions).

The dynamics of $\sigma_x(t)$ can be subdivided into three subregions:

$$\sigma_x^2(t) \simeq \begin{cases} 2\,\varepsilon\, t & 0 < t < t^* \\ B\, t^\gamma & t^* < t < t^{**} \\ 2\,\varepsilon^*\, t & t \gg t^{**}\,, \end{cases} \tag{82}$$

where B is a constant independent of time.

Initially ($t < t^*$), an initial transient occurs controlled by diffusion. Consequently, $\sigma_x^2(t) = 2\,\varepsilon\, t$. Asymptotically, i.e., for $t \gg t^{**}$, the long-term or large-distance regime sets up and, consequently, $\sigma_x^2(t) \simeq 2\,\varepsilon^*\, t$, where ε^* is the reciprocal of the dispersion Peclét number thoroughly analyzed in the previous two sections.

The intermediate regime, occurring for $t \in (t^*,t^{**})$, is characterized by a superdiffusive scaling, $\sigma_x^2(t) \sim t^\gamma$, with an exponent $\gamma \geqslant 2$ that depends on the initial transverse distribution. For an initial uniform transverse distribution (U condition), line (a) in Fig. 17, a ballistic dispersion is observed, namely $\gamma = 2$, while for localized initial transverse distributions (L conditions), lines (b) and (c) in Figs. 17, a superballistic anomalous dispersion occurs, characterized by an exponent $\gamma = 3$. The manifestation of this superballistic behavior becomes more pronounced as Pe increases as depicted in Fig. 18. While at $\varepsilon = 8 \times 10^{-3}$, line (a) in Fig. 18, corresponding to Pe $= 125$, $\sigma_x^2(t)$ starts to deviate from the superballistic scaling at $t^{**} \simeq 2 \times 10^4$, at $\varepsilon = 6 \times 10^{-3}$ (Pe $= 166.67$), line (b) in this figure, this regime in neatly observable over more than two decades $t \in (t^* = 10^3, 10^5)$, implying $t^{**} \gg 10^5$.

The spatial structure of the probability density function as it evolves along the channel at intermediate scales is depicted in Fig. 19 for the two classes of initial conditions considered.

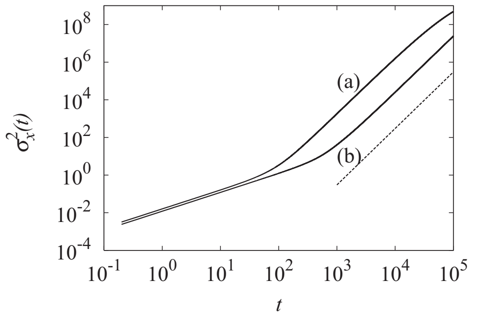

FIG. 18. $\sigma_x^2(t)$ vs t for $k = 3$, $\nu = 1$. Solid lines reproduce the results of Langevin simulations: (a) $\varepsilon = 8 \times 10^{-3}$ and (b) $\varepsilon = 6 \times 10^{-3}$. The dashed line represents the scaling $\sigma_x^2(t) \sim t^3$.

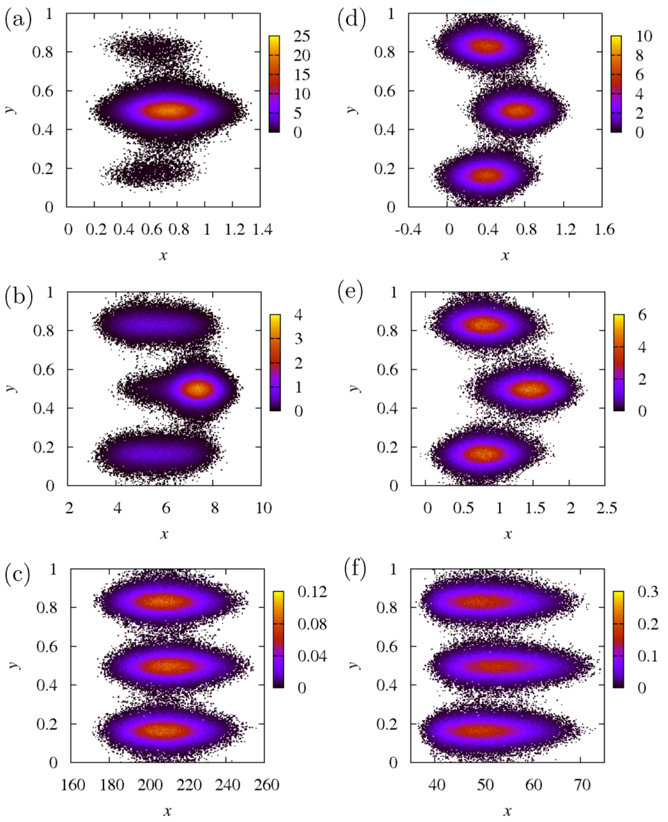

FIG. 19. (Color online) Contour plot of $p(x,y,t)$ at $\varepsilon = 3 \times 10^{-2}$ for two different initial conditions at different time instants. Panels (a) to (c): L conditions, $y_c = 1/2$, at $t = 0.5$ (a), $t = 5$ (b), and $t = 100$ (c). Panels (d) to (f): U conditions at $t = 0.5$ (d), $t = 1$ (e), and $t = 50$ (f).

Two-dimensional plots of $p(x,y,t)$ for Pe $= 100$, corresponding to the σ_x^2 data depicted in Fig. 17 are reported in Fig. 20 starting from a L condition at $y_c = 1/2$.

The difference between the two intermediate scalings starting from U and L initial conditions is related to qualitatively different relaxation properties in the transverse direction. In U conditions, the transverse relaxation is very fast as uniform initial conditions allow particles to reach the stable nodes and to distribute according to the stationary Frobenius distribution $\psi_0(y)$ without crossing potential barriers. In this case the intermediate scaling region is associated exclusively to the axial relaxation towards a Gaussian profile. Consequently, in the intermediate-scale region it can be assumed that $p_y(y,t) = \psi_0(y)$.

At intermediate time scales, axial diffusion is negligible with respect to the deterministic motion induced by the flow. This means that the axial dynamics of a particle located in the transverse position y can be approximated for $t < t^{**}$ by $x_y(t) = u(y)t$ and, consequently,

$$\sigma_x^2(t) = \int_0^1 \psi_0(y)\,[V_e t - u(y)t]^2\, dy = S_2\, t^2, \tag{83}$$

where $S_2 = \int_0^1 \psi_0(y)\,[V_e - u(y)]^2 dy$. For large Pe values, this expression can be further simplified by approximating $\psi_0(y)$ with a combination of δ functions centered at the stable nodes

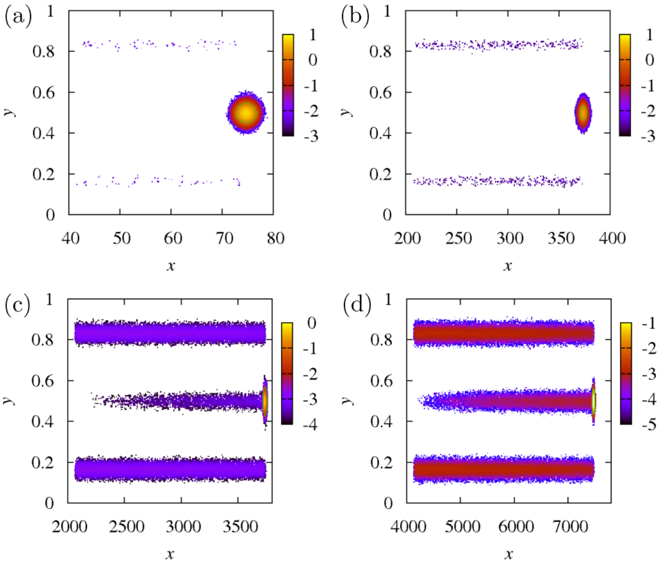

FIG. 20. (Color online) Contour plot of the logarithm of $p(x,y,t)$ at $\varepsilon = 10^{-2}$ at different time instants. Panels (a) $t = 50$, (b) $t = 250$, (c) $t = 2500$, (d) $t = 5000$.

$y^*_{n,k}$, and V_e with V_e^*, so the prefactor S_2 can be expressed as:

$$S_2 = \frac{1}{k} \sum_{n=0}^{k-1} [V_e - u(y^*_{n,k})]^2. \tag{84}$$

Figure 21(a) depicts the comparison of Langevin simulations and the theoretical prediction based on Eqs. (83) and (84) where the asymptotic expression (84) for S_2 has been used at $\varepsilon = 5 \times 10^{-3}$ for two values of k. It can be observed that the agreement of the simple model (84) with the simulations of particle motion is fully satisfactory even for relatively small Pe values (Pe $\geqslant 200$). This is further supported by the comparison of the estimate of the prefactor S_2 obtained from stochastic simulations and expression (84) depicted in Fig. 21(b).

L conditions are slightly more difficult to handle, as a localized initial distribution implies that particle ensembles achieve the stationary transversal distribution performing a series of tunneling processes across the potential barriers separating two neighboring stable states.

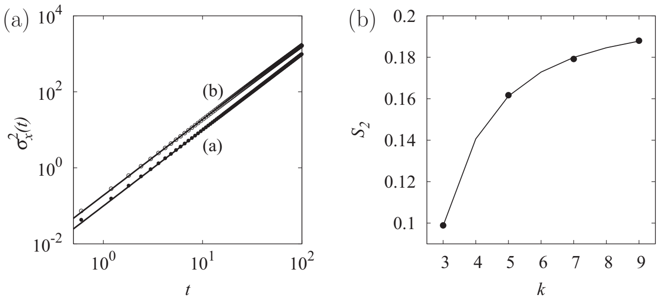

FIG. 21. (a) $\sigma_x^2(t)$ vs t for $\varepsilon = 5 \times 10^{-3}$, $\nu = 1$, at intermediate time scales starting from an initially uniform transverse distribution. Symbols represent the results of Langevin simulations, solid lines the theoretical predictions based on Eqs. (83) and (84). Line (a) and (●): $k = 3$, line (b) and (○): $k = 9$. (b) Prefactor S_2 vs k. Solid line represents the theoretical prediction in Eq. (84) and symbols (●) the value of S_2 obtained from the fitting of Langevin simulations at $\varepsilon = 5 \times 10^{-3}$.

In order to simplify the analysis, consider the case $k = 3$ where $y_c = 1/2$, i.e., where the particles are injected at the midpoint stable node. The intermediate scaling behavior $\sigma_x^2(t) \sim t^3$, observed under L conditions, is the combination of ballistic dispersion deriving from axial velocity differences at the stable nodes and the tunneling dynamics in the transverse direction to achieve the stable transversal distribution expressed by the Frobenius eigenfunction $\psi_0(y)$.

Let $y^{u,*}_{n,k}$, $n = 1, \ldots k-1$ be the unstable nodes separating $y^*_{n-1,k}$ from $y^*_{n,k}$, and set $y^{u,*}_{0,k} = 0$, $y^{u,*}_{k,k} = 1$. Within the basin of attraction of each stable node the convergence towards $y^*_{n,k}$ is fast compared to the characteristic time scales of the intermediate regime, which is order of $\mathcal{O}(t^{**} - t^*)$. Therefore, to achieve a physical and qualitative explanation of the anomalous behavior of $\sigma_x^2(t)$, it is possible to use a very crude approximation for $p_y(y,t)$, as a combination of δ functions centered at the stable nodes (as developed for U conditions),

$$p_y(y,t) = \sum_{n=0}^{k-1} \pi_n(t)\, \delta(y - y^*_{n,k}), \tag{85}$$

where $\pi_n(t) \geqslant 0, n = 0, \ldots, k-1, \sum_{n=1}^{k-1} \pi_n(t) = 1$, represent the probability of finding a particle in the attraction interval $(y^{u,*}_{n,k}, y^{u,*}_{n+1,k})$ of the stable node $y^*_{n,k}$, i.e.,

$$\pi_n(t) = \int_{y^{u,*}_{n,k}}^{y^{u,*}_{n+1,k}} p_y(y,t)\, dy. \tag{86}$$

For the case study considered ($k = 3$), $\pi_0(0) = \pi_2(0) = 0$, $\pi_1(0) = 1$.

The difference with respect to the U conditions is that now $\pi_n(t)$ depends on time t, and also the time dependence of the mean axial velocity $V(t)$ should be taken into account. This transient effect, enhanced by particle tunneling, makes $\sigma_x^2(t)$ to deviate from purely ballistic dispersion.

The time evolution of $\pi_0(t) = \pi_2(t)$ (these two quantities are equal by symmetry for the case study considered) is rather easy to estimate as it is related to particle tunneling across the unstable nodes $y^{u,*}_{1,3}$ [for $\pi_0(t)$] and $y^{u,*}_{2,3}$ [for $\pi_2(t)$].

From a macroscopic balance over the attraction interval of $y^*_{0,k}$, it follows that $\pi_0(t)$ equals the time integral of the particle flux (tunneling flux) at the unstable node $y^{u,*}_{1,3}$, i.e.,

$$\pi_0(t) = \int_0^t J_{\text{tun}}(\tau)\, d\tau, \tag{87}$$

where

$$J_{\text{tun}}(t) = \varepsilon\, \partial_y p(y,t)|_{y=y^{u,*}_{1,3}}, \tag{88}$$

where $p(y,t)$ is the solution of the transverse advection-diffusion dynamics (33) equipped with homogeneous Neumann conditions at the end points and with the initial condition $p_y(y,0) = \delta(y - y_c)$, $y_c = 1/2$.

It can be shown numerically, integrating Eq. (33), that $J_{\text{tun}}(t)$ in the intermediate-scale region, i.e., apart of a very early initial dynamics irrelevant for $t > t^*$, is practically

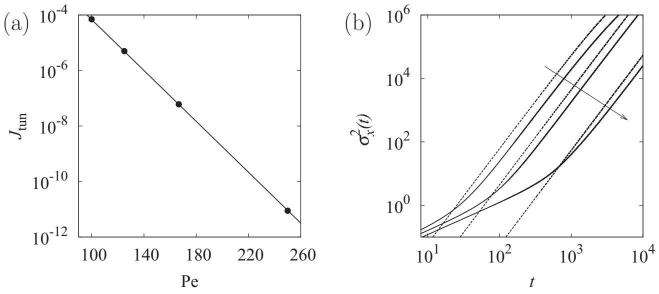

FIG. 22. (a) Tunneling flux $J_{\rm tun}$ vs Pe: symbols (●) represent the results of numerical simulations using the transversal transport equation (33); the solid line (b) is the exponential behavior $J_{\rm tun} = Ae^{-F{\rm Pe}}$, with $F = 0.1055$. (b) Comparison of the theoretical predictions (dashed lines) based on Eq. (90) with Langevin simulations (solid lines). The arrow indicates decreasing values of $\varepsilon = 10^{-2}, 8 \times 10^{-3}, 6 \times 10^{-3}$.

constant, so Eq. (87) simplifies as:

$$\pi_0(t) = J_{\rm tun}\, t. \tag{89}$$

Figure 22(a) depicts the behavior of $J_{\rm tun}$ vs Pe. As expected from rate-process theory [33], $J_{\rm tun} \sim e^{-F\,{\rm Pe}}$, where F is a constant.

Under L conditions for $k = 3$, it follows from the impulsive approximation (85) that:

$$\sigma_x^2(t) = \sum_{k=0}^{2} \pi_n(t)\,[V(t)\,t - u(y^*_{n,k})\,t]^2, \tag{90}$$

where

$$V(t) = \sum_{n=0}^{2} \pi_n(t)\,u(y^*_{n,k}). \tag{91}$$

Enforcing Eq. (89), it follows that:

$$\sigma_x^2(t) \simeq S_3\,t^3 \sim J_{\rm tun}\,t^3, \tag{92}$$

providing a theoretical explanation for the superballistic dispersion enhanced by tunneling.

Figure 22(b) depicts the theoretical prediction for $\sigma_x^2(t)$ based on Eqs. (89)–(91) compared with Langevin data. We use in Eq. (89) the value of $J_{\rm tun}$ obtained from the solution of the transverse transport dynamics (33). The theoretical prediction overestimates the scaling prefactor S_3 by a factor of 2 at $\varepsilon = 10^{-2}$. This overestimation is due to the "crude" impulsive approximation (85) for $p_y(y,t)$ that is certainly less accurate for small Pe values, as it corresponds to the asymptotic behavior for Pe → ∞. Indeed, as Pe increases, the prediction for the prefactor S_3 improves [see Fig. 22(b)]. In point of fact, Eq. (85) could be refined simply replacing the δ functions with the corresponding Gaussian pulses of finite width, improving, as a by-product, the estimate of S_3. In any case, this tedious calculation does not add anything new to the physical understanding of the phenomenon and is left to the scrupulous reader as an algebraic exercise.

VII. CONCLUDING REMARKS

This article has developed a comprehensive analysis of particle transport and dispersion in two-dimensional acoustophoretic channels. The extension to three-dimensional devices, also in the presence of secondary vortices, will be developed elsewhere.

The model system considered represents a simple but absolutely nontrivial example of interaction between solenoidal and irrotational velocity components with noise. Theoretical analysis of the b-field equation has provided a complete qualitative and quantitative theoretical prediction of the asymptotic dispersive behavior based on the localization properties of the steady field $b(y)$. This analysis is conceptually similar to the study of eigenfunction localization in simple mixing systems possessing a convection-enhanced spectral branch [6].

Transient dynamics of the mean-square axial displacement has revealed anomalous superdiffusive properties that have been interpreted by theoretical arguments (tunneling across potential barriers).

As this simple model system has shown interesting and new scaling properties in the dispersive dynamics, it is expected that the interplay between solenoidal and irrotational fields coupled with stochastic fluctuations (diffusion) in more complex settings will lead to a manifold of different physical phenomenologies still to be discovered and characterized both in the light of a comprehensive theory of stochastic fluctuations in the presence of deterministic vector fields and for their potential use in microtechnological applications.

APPENDIX

Consider Eq. (26), multiply it by $b(y)$ and integrate over y in the interval [0,1]:

$$\int_0^1 \psi_0(y)[V_e - u(y)]\,b(y)\,dy = \int_0^1 b(y)\,\mathcal{L}_y[\psi_0(y)\,b(y)]\,dy. \tag{A1}$$

Set $s(y) = \nu \sin(2\pi k y)$, so

$$\begin{aligned}\int_0^1 & b(y)\,\mathcal{L}_y[\psi_0(y)\,b(y)]\,dy\\ &= \int_0^1 b(y)\big\{-\partial_y[s(y)\psi_0(y)b(y)] + \varepsilon\partial_y^2[\psi_0(y)b(y)]\big\}dy\\ &= \underbrace{\int_0^1 \partial_y\{b(y)[-s(y)\psi_0(y)b(y)] + \varepsilon\partial_y[\psi_0(y)b(y)]\}dy}_{=0}\\ &\quad + \int_0^1 \{s(y)\psi_0(y)b(y)\partial_y b(y) - \varepsilon\partial_y b(y)\,\partial_y[\psi_0(y)b(y)]\}\,dy\\ &= -\varepsilon\int_0^1 \psi_0(y)[\partial_y b(y)]^2\,dy + \int_0^1 b(y)\,\partial_y b(y)[s(y)\psi_0(y)\\ &\quad - \varepsilon\partial_y\psi_0(y)]dy.\end{aligned} \tag{A2}$$

But $\psi_0(y)$ is the Frobenius eigenfunction, the solution of equation $\mathcal{L}_y[\psi_0(y)] = 0$. Therefore, $-s(y)\psi_0(y) + \varepsilon\partial_y\psi_0(y) = A = \text{const}$. Because of the boundary conditions, since $s(y)|_{y=0,1} = 0$, the constant A is identically vanishing, which implies that the second integral in Eq. (A2) is also vanishing. Thus Eq. (31) follows.

[1] J. Zinn-Justin, *Quantum Field Theory and Critical Phenomena* (Oxford University Press, Oxford, 2002); H. Kleinert, *Gauge Fields in Condensed Matter*, Vol. I (World Scientific, Singapore, 1989).

[2] M. Doi and S. F. Edwards, *The Theory of Polymer Dynamics* (Clarendon Press, Oxford, 1989).

[3] S. Chandrasekhar, Rev. Mod. Phys. **15**, 1 (1943).

[4] E. Nelson, *Quantum Fluctuations* (Princeton University Press, Princeton, NJ, 1985); A. O. Caldeira and A. J. Leggett, Physica A **121**, 587 (1983).

[5] H. Bruus, *Theoretical Microfluidics* (Oxford University Press, Oxford, 2008).

[6] M. Giona, A. Adrover, S. Cerbelli, and V. Vitacolonna, Phys. Rev. Lett. **92**, 114101 (2004); M. Giona, S. Cerbelli, and V. Vitacolonna, J. Fluid. Mech. **513**, 221 (2004); M. Giona, S. Cerbelli, and F. Garofalo, Europhys. Lett. **83**, 34001 (2008); G. Froyland and K. Padberg, Physica D **238**, 1507 (2009); G. Froyland, O. Junge, and P. Koltai, SIAM J. Numer. Anal. **51**, 223 (2013).

[7] R. Aris, Proc. R. Soc. London A **235**, 67 (1956).

[8] A. J. Majda and R. M. McLaughlin, Stud. Appl. Math. **89**, 245 (1993).

[9] A. J. Majda and P. R. Kramer, Phys. Rep. **314**, 237 (1999).

[10] L. Gammaitoni, P. Hänggi, P. Jung, and F. Marchesoni, Rev. Mod. Phys. **70**, 223 (1998).

[11] P. Reimann, Phys. Rep. **361**, 57 (2002).

[12] P. Reimann, C. Van den Broeck, H. Linke, P. Hänggi, J. M. Rubi, and A. Perez-Madrid, Phys. Rev. Lett. **87**, 010602 (2001); Phys. Rev. E **65**, 031104 (2002).

[13] J. Um, H. Hong, F. Marchesoni, and H. Park, Phys. Rev. Lett. **108**, 060601 (2012).

[14] G. Schwarz, *Hodgle Decomposition: A Method for Solving Boundary Value Problems* (Springer-Verlag, Berlin, 1995).

[15] S. Cerbelli, Phys. Rev. E **87**, 060102 (2013).

[16] P. K. Ghosh, P. Hänggi, F. Marchesoni, S. Martens, F. Nori, L. Schimansky-Geier, and G. Schmid, Phys. Rev. E **85**, 011101 (2012).

[17] F. Petersson, L. Aberg, A. M. Swärd-Nilsson, and T. Laurell, Anal. Chem. **79**, 5117 (2007).

[18] J. Shi, H. Huangm, Z. Stratton, Y. Huang, and T. J. Huang, Lab Chip **9**, 3354 (2009).

[19] R. Guldiken, M.-C. Jo, N. D. Gallant, U. Demirci, and J. Zhe, Sensors **12**, 905 (2012).

[20] D. Hartono, Y. Liu, P. L. Tan, X. Y. S. Then, L.-Y. L. Yung, and K.-M. Lim, Lab Chip **11**, 4072 (2011).

[21] J. M. Nitsche and H. Brenner, J. Chem. Phys. **89**, 7510 (1988).

[22] H. Brenner and D. A. Edwards, *Macrotransport Processes* (Butterworth-Heinemann, Boston, 1993).

[23] S. Cerbelli, M. Giona, and F. Garofalo, Microfluid. Nanofluid. **15**, 431 (2013).

[24] H. Bruus, Lab Chip **11**, 3742 (2011); P. Glynne-Jones and M. Hill, *ibid.* **13**, 1003 (2013); T. Laurell and A. Lenshof (eds.), *Microscale Acoustofluidics* (Royal Society of Chemistry, Cambridge, 2015).

[25] L. V. King, Phys. Trans. Royal Soc. London A **147**, 212 (1934).

[26] L. P. Gorkov, Sov. Phys. Dokl. **6**, 773 (1962).

[27] A. A. Doinikov, J. Fluid Mech. **267**, 1 (1994).

[28] S. D. Danilov and M. A. Mironov, J. Acoust. Soc. Am. **107**, 143 (2000).

[29] M. Settnes and H. Bruus, Phys. Rev. E **85**, 016327 (2012).

[30] P. B. Muller, M. Rossi, A. G. Marin, R. Barnkob, P. Augustsson, T. Laurell, C. J. Kähler, and H. Bruus, Phys. Rev. E **88**, 023006 (2013).

[31] A. Bensoussan, J.-L. Lions, and G. Papanicolau, *Asymptotic Analysis for Periodic Structures* (AMS Chelsea, Providence RI, 1978).

[32] F. Garofalo, Microfluid. Nanofluid. **18**, 367 (2015).

[33] H. A. Kramers, Physica **7**, 284 (1940).